MATERIALS SCIENCE

Controlling thermoreversibility and hole conductivity in thermoresponsive ionic biogels using phase morphology for neurohaptics

Ankan Dutta[1,2,3,4]*, Md Abu Sayeed Biswas[2], Ethan Gerhard[5], Mayukh Das[2], Long Meng[1], Wanqing Zhang[2], Wenjie Li[6,7], Arantza Moreno Calva[2,8], Shakul Pathak[9], Jia-Yu Yang[2,10], Junyi Yin[11], Jordan Meyet[12], Shuvendu Das[2], Bed Poudel[6], Abu Musa Abdullah[2], Yuju Che[2,13], Cheng-Hsin Chuang[10], Jian Yang[14], Sihong Wang[11,15,16], Xiaogang Hu[1,3,17], Saptarshi Das[2,6,12,18], Huanyu Cheng[1,2,3,5,6,12,18]*

Integrating thermoreversibility with electrical conductivity in a unified hydrogel platform enables long-term, reusable through-hair neural interfaces. However, achieving both simultaneously remains challenging, as thermoreversibility demands network reorganization while conductivity necessitates network percolation. Here, we engineer phase morphology by controlling the components' viscoelastic state during mixing. Ionically conductive nucleated morphologies illustrated by liquid-liquid phase separation exhibit rapid thermoreversibility, whereas electrically conductive bicontinuous phases demonstrated by viscoelastic phase separation achieve a marginal gel-sol transition and an ultralow storage modulus of ~1.7 kilopascals while simultaneously achieving a conductivity of 7.5 siemens per centimeter or transconductance of 5.1 millisiemens in an organic electrochemical transistor. Below this threshold, systems resemble nucleated behavior, whereas above it, superior semiconducting properties emerge, but phase transition capability is lost. These materials enable reusable through-hair neural interfaces to maintain low skin contact impedance of 1.6 kohm·cm^2 across different hair types for 3 days, facilitating stable event-related desynchronization detection during mechanical and electrical haptic sensation for personalized haptics.

INTRODUCTION

Long-term, reusable through-hair neural interfaces could advance personalized haptics for augmented and virtual reality by enabling continuous monitoring of neural responses during stimulation, providing objective inputs for closed-loop feedback systems that better emulate naturalistic sensation and interaction (*1*, *2*). Yet despite advances in hydrogel-based electroencephalogram (EEG) electrodes, practical deployment remains limited by two coupled failure modes: (i) inefficient coupling through hair and (ii) long-term signal drift driven by dehydration. The first constraint can be resolved by thermoresponsive hydrogels, particularly thermoreversible hydrogels (*3*, *4*), whose viscoelastic network organization, and therefore viscosity, modulus, and adhesion, can be actively programmed by temperature to enable transition between a flowable state for hair infiltration and an adhesive, conformal state that ensures stable contact under motion. On the other hand, analyzing long-term effects like neuroplasticity during closed-loop haptics further requires that the hydrogel maintain stable electrical transport independent of hydration state, so that the skin contact impedance and recording fidelity do not degrade over hours to days—the second constraint (*5*–*7*). Electrically conducting and semiconducting hydrogels can provide tissue-compliant bioelectronics with stable, efficient carrier transport (*8*, *9*), whereas ionic liquid–based conductors offer an alternative route to dehydration tolerance by leveraging the ionic liquid's low volatility (low vapor pressure). Therefore, a material platform that couples thermoreversibility with dehydration-tolerant conductivity (electronic or ionic) would directly address the signal stability requirements of long-term, reusable through-hair neural interfaces.

Ionic liquid–based ionically conductive materials are a promising route to dehydration-tolerant neural interfaces. Yet during extended wear, electrode-skin coupling can still evolve, as sweat influx, hair oil, and water loss progressively modify the bulk ionic conductivity and thereby shift the effective skin contact impedance over time. Although such ionic conduction remains a plausible basis for stable interfacing, these limitations suggest that an additional transport pathway may be needed to maintain robust coupling under prolonged physiological variability. By introducing an electronically percolated pathway, charge transport becomes increasingly governed by a coherent, largely resistive electronic network, reducing sensitivity to fluctuations in ionic strength and dehydration and thereby stabilizing interfacial coupling (*10*). But unfortunately, engineering

[1]Department of Mechanical Engineering, The Pennsylvania State University, University Park, PA 16802, USA. [2]Department of Engineering Science and Mechanics, The Pennsylvania State University, University Park, PA 16802, USA. [3]Center for Neural Engineering, The Pennsylvania State University, University Park, PA 16802, USA. [4]Broad Institute of MIT and Harvard, Cambridge, MA 02142, USA. [5]Department of Biomedical Engineering, The Pennsylvania State University, University Park, PA 16802, USA. [6]Department of Materials Science and Engineering, The Pennsylvania State University, University Park, PA 16802, USA. [7]Department of Biochemistry, Chemistry and Physics, Georgia Southern University, Statesboro, GA 30458, USA. [8]Department of Biomedical Engineering, Universidad Iberoamericana, CDMX, 01219, Mexico. [9]Department of Chemical Engineering, Massachusetts Institute of Technology, Cambridge, MA 02142, USA. [10]Institute of Medical Science and Technology, National Sun Yat-sen University, College of Medicine, Kaohsiung 80424, Taiwan. [11]Pritzker School of Molecular Engineering, University of Chicago, Chicago, IL 60637, USA. [12]Material Research Institute, The Pennsylvania State University, University Park, PA 16802, USA. [13]Marine College, Shandong University (Weihai), Weihai, 264209, China. [14]Department of Materials Science and Engineering, Westlake University, Hangzhou, Zhejiang 310030, P.R. China. [15]Nanoscience and Technology Division and Center for Molecular Engineering, Argonne National Laboratory, Lemont, IL 60439, USA. [16]CZ Biohub Chicago LLC, Chicago, IL 60642, USA. [17]Department of Kinesiology, The Pennsylvania State University, University Park, PA 16802, USA. [18]Department of Electrical Engineering, The Pennsylvania State University, University Park, PA 16802, USA.
*Corresponding author. Email: amd7627@psu.edu (A.D.); huanyu.cheng@psu.edu (H.C.)

electrically conducting systems to simultaneously retain thermoreversibility remains a profound challenge, as these functionalities arise from fundamentally antagonistic design requirements. Efficient thermoreversibility relies on dynamic, often reversible noncovalent interactions such as hydrogen bonding or hydrophobicity that facilitate sol-gel transitions in response to a thermal stimulus (*3*, *4*). In contrast, efficient electronic conductivity requires percolated, π-conjugated polymeric networks that resist network rearrangement under thermal cycling. Typically, conducting or semiconducting hydrogels have relied on chemically crosslinked networks (*8*, *9*, *11*). Only a limited number of physically crosslinked systems have been reported (*12*), and thermoresponsive electrically conducting hydrogels, particularly those exhibiting thermoreversible gel-sol transitions, remain largely unexplored (fig. S1). To address this, we propose combining a physically crosslinked, thermoreversible hydrogel matrix, such as gelatin or agarose, with an intrinsically conducting but insoluble polymeric network, exemplified by poly(3,4-ethylenedioxythiophene) polystyrene sulfonate (PEDOT:PSS), and use PEDOT phase morphology as the design tool to balance thermoreversibility and charge transport, thereby conductivity. In PEDOT:PSS-based hydrogels, PEDOT-rich domains typically phase-separate to form isolated crystalline conducting domains in the ionic conductive matrix, resulting in a nonpercolating or nucleated phase morphology (*8*, *12*–*16*). Although these morphologies are necessary for thermoreversibility, they often lack coherent electrical conductivity. To improve electrical conductivity, recent efforts have exploited increased solubility or hydrophilicity of polymeric semiconductors or conductors (*10*, *14*, *16*, *17*), but consequently, the covalent nature of these systems lacks thermoreversibility. Thermoreversible conducting hydrogels via supramolecular/colloidal strategies can result in conducting gels, but electronic transport becomes secondary to ionic conduction as a robust percolated coherent pathway is not formed, thus limiting their conductivity and resulting in lack of semiconductivity (*18*, *19*). Embedding conductive fillers (e.g., carbon nanotubes and silver nanowires/flakes) into thermoresponsive gels faces an inherent conductivity-viscoelastic trade-off, as achieving reliable electronic percolation requires a high loading/aggregation of filler network rather than a tunable phase morphology, i.e., for a fixed weight concentration, the percolation network is fixed and not controllable (*20*, *21*). Insights into processing-structure-property relationships (by leveraging solvent-driven phase separation governed by insolubility) have provided pathways toward achieving bicontinuous morphologies, wherein hydrophobic PEDOT-rich and hydrophilic domains independently percolate, facilitating simultaneous electronic and ionic conduction (*22*). However, such permanent bicontinuous networks lack gel-sol transition and thereby any thermoreversibility, due to the formation of arrested, bicontinuous domains that resist redissolution or network reformation upon thermal cycling (*3*).

Here, we address the central trade-off between polymeric percolation required for electronic charge transport and network lability required for thermoreversibility by engineering the PEDOT-rich phase to be continuous yet minimally constrained (*10*). Specifically, we aim to operate at the lowest polymer loading, i.e., percolation threshold, enabling a marginally connected bicontinuous morphology in which the conducting backbone is sufficiently continuous for long-range charge transport yet sparse and labile enough to undergo reversible gel-sol transitions without evolving into a permanently arrested scaffold. In contrast, ionically dominated transport does not require a polymeric percolation, as charge is carried by mobile ions; therefore, a simple nucleated PEDOT phase showing liquid-liquid phase separation (LLPS) can be beneficial in ionically conductive systems. The same formulation can be redirected toward viscoelastic phase separation (VPS)–like behavior resembling network microstructure, if the viscoelastic state at the time of mixing becomes sufficiently asymmetric. This general principle is reminiscent of biological membraneless organelles, whose mesoscale organization emerges through LLPS- or VPS-governed phase dynamics (*23*–*26*). In LLPS, demixing occurs in a liquid-like medium and proceeds by nucleation growth to reduce the total free energy, with interfacial tension selecting droplet-like morphologies (for off-critical compositions) by minimizing the interfacial area. As a result, the minority phase typically does not form a continuous phase unless the composition lies near the critical point for spinodal decomposition (*23*, *24*, *26*). On the other hand, VPS arises in dynamically asymmetric mixtures in which one phase relaxes stress much more slowly than the other (e.g., a stress-bearing gel and a low viscous fluid component) (*27*–*29*). In VPS, viscoelastic stresses couple to diffusion and morphology are governed by asymmetric stress division rather than interfacial tension alone, which can drive the network formation for stress-bearing minority phase. These concepts provide a useful blueprint for our material design: The percolating network exhibiting electrically conducting or semiconductivity can be exemplified by VPS due to their reversible sparse network-like formation, whereas ionically conductive system can be demonstrated by LLPS-like nucleated phases without any coherent transport.

We demonstrate an ionic biogel system composed of PEDOT:PSS/ionic liquid/salt (ionic phase) and gelatin-glycerol or agarose-glycerol (biogel phase) systems with two types of polymer mixing sequences: (i) nucleated (PEDOT:PSS in aqueous phase mixed with low-viscosity biogel phase) with a stable configuration with isolated PEDOT phases, similar to LLPS, and (ii) bicontinuous (PEDOT:PSS in aqueous phase mixed with highly viscous gelled biogel phase) with a kinetically constrained percolated PEDOT phase, similar to VPS (Fig. 1A, figs. S2 to S10, and note S1). The nucleated systems (NC) show highly efficient, rapid thermoreversibility but are dominated by mobile ion–assisted conduction, whereas the bicontinuous systems with polymeric concentration below the percolation threshold result in nonpercolated phase morphology (BC-NP) and show similar rheological characteristics, phase dynamics, and conductivity as NC. However, bicontinuous systems with polymeric concentration above the percolation threshold can be categorized as marginally percolated (BC-MP) and permanently percolated (BC-PP). We could engineer the BC-MP system within a very small polymeric concentration [~100 to 125 w/w% of aqueous PEDOT:PSS with respect to (w.r.t.) biogel] with simultaneous semiconducting property and a gel-sol phase transition (loss tangent $\tan\delta \approx 1$) and ultralow storage modulus (<1 kPa) (summarized in table S1). Above this concentration map, the bicontinuous system forms a quasi-permanent scaffold-like network with percolating PEDOT phases, categorized as BC-PP. Moreover, the bicontinuous systems become a layered heterogeneous system when there is no mixing, highlighting a highly conductive system analogous to a degenerately doped semiconductor. Both the NC (ionic-liquid–stabilized ionic conduction) and BC-MP (marginally electronically percolated) enable a reusable, robust neural interface with low skin contact impedance of 1.6 kohm·cm^2 at 1 kHz across eight different hair types, maintained more than 3 days to establish a long-term objective assessment of mechanical and electrical stimulations using event-related desynchronization (ERD). Even

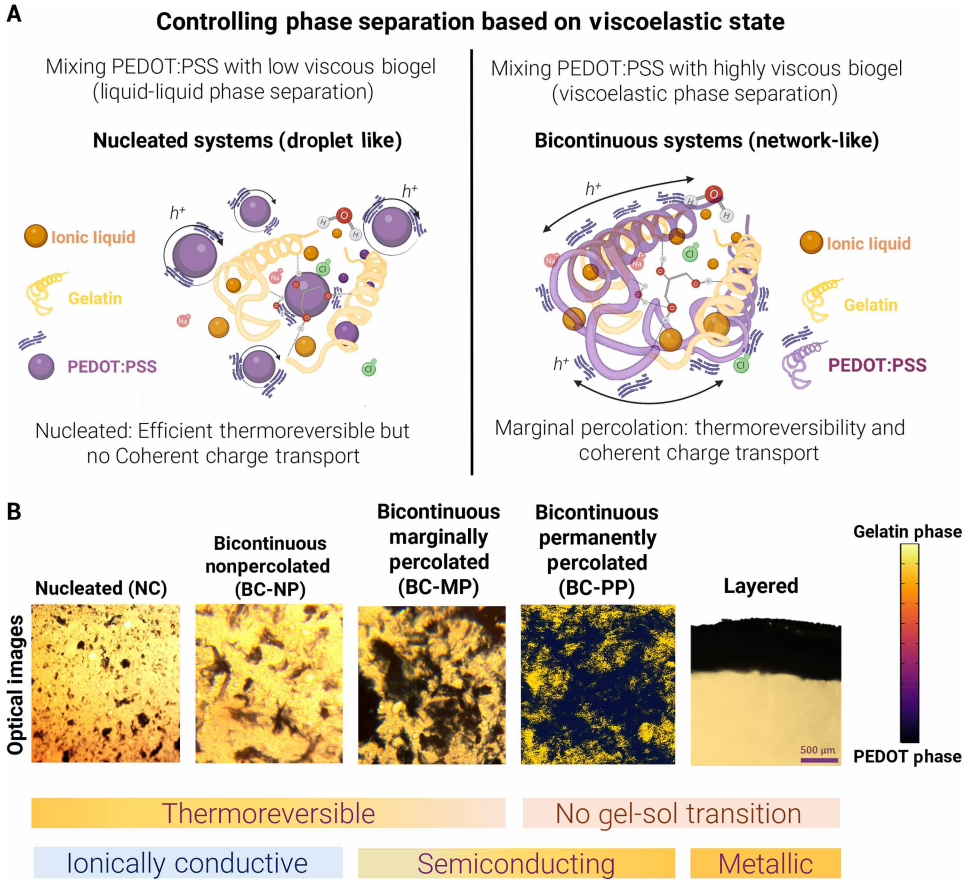

Fig. 1. Schematic illustration of the material design of ionic biogel based on the mixing strategy—NC, BC-NP, BC-MP, BC-PP, and layered (bicontinuous system without mixing). (**A**) NC mimicking LLPS forms isolated PEDOT domains, forming a stable thermodynamic system, where increasing PEDOT concentration only results in an increased number or size of isolated PEDOT domains with no charge transport. Bicontinuous system mimicking VPS forms a network-like phase morphology, where the increased PEDOT concentration (more than percolation threshold) changes the phase morphology from nonpercolating (BC-NP) to marginally percolating (BC-MP) to permanently percolating (BC-PP) to facilitate a coherent charge pathway. BC-NP shows ionically dominated charge transport like NC, whereas BC-MP and BC-PP enable electrical conductivity and semiconductivity. However, the thermoreversibility characteristics follow the opposite trend: BC-NP is thermoreversible, whereas BC-MP shows a marginal gel-sol transition and BC-PP forms a permanent scaffold. (**B**) The optical images of NC, BC-NP, and BC-PP showing the PEDOT phase and gelatin-phase morphology. NC follows a LLPS-inspired droplet-like morphology with a PEDOT phase correlation length of 172 μm, whereas BC-NP has 474 μm and BC-MP has around 1250 μm.

after 10 days of reusability, the BC-MP gel exhibits a smaller impedance increase (~500 ohm·cm^2), whereas the NC changes by ~1500 ohm·cm^2, indicating greater long-term interfacial stability for the electronically percolated morphology.

RESULTS

Kinetics of mixing in ionic biogel

Ionic biogels were prepared using two mixing sequences that differ only in the mechanical state of the biogel phase at the moment PEDOT:PSS is introduced, thereby selecting distinct phase separation pathways and, consequently, distinct microstructures. Quantitative image analyses of the two resulting morphologies shows distinct two-point correlation length (ξ) of PEDOT phase, largest PEDOT domain length/area, and distribution variance: ξ increases from NC (172 μm) to BC-NP (474 μm) to BC-MP (1250 μm), the maximum PEDOT domain size follows BC-PP > BC-MP > BC-NP > NC, and the variance is high in BC-MP/BC-PP but low in NC/BC-NP, consistent with a transition from droplet-like (distinct domains) to network-like (connected domains) microstructure (Fig. 1B and fig. S11). In the nucleated route, PEDOT:PSS is first mixed with salt and ionic liquid and only then mixed with glycerol and gelatin or agarose. Phase separation is therefore initiated while the matrix remains low viscosity (no stress-bearing matrix), and subsequent gelatin or agarose gelation primarily arrests the droplet morphology, following LLPS. In the bicontinuous route, gelatin (or agarose)–glycerol–salt ionic liquid, i.e., biogel phase is first allowed to partially gel into a viscous organo-ionogel and aqueous PEDOT:PSS is introduced after ~5 min, so demixing proceeds inside a stress-bearing biogel phase and is then kinetically arrested into an amorphous state. Crucially, the relevant dynamic asymmetry is temperature dependent in our system: Upon heating, the biogel phase undergoes a gel-sol transition locally, whereas the PEDOT-rich phase can exhibit slower mechanical relaxation due to an increase in its elastic modulus during plasticization or doping by glycerol or ionic liquid. Under such conditions, the identity of the dominant stress-bearing phase inverted during the thermal cycle: The PEDOT phase becomes the minority stress-bearing phase (*27*). This maps onto Tanaka's VPS theory

(*28*), where the composition field $\phi(\mathbf{x}, t)$ (volume fraction of the slow, PEDOT-rich component) evolves

$$\frac{\partial \phi}{\partial t} = -\nabla(\phi v) - \nabla \cdot \frac{\phi(1-\phi)^2}{\zeta(\phi)}\left[\nabla \cdot \Pi - \nabla \cdot \sigma^{(1)} + \frac{\phi}{1-\phi}\nabla \cdot \sigma^{(2)}\right] \quad (1)$$

where $\zeta(\phi)$ is the intercomponent friction, v is the polymer velocity, Π is the osmotic stress derived from the mixing free energy, and $\sigma^{(1)}$ and $\sigma^{(2)}$ are viscoelastic stresses carried by the PEDOT-rich component and gelatin network, respectively. VPS emerges specifically under strong dynamic asymmetry $\sigma^{(1)} \gg \sigma^{(2)}$ and cannot relax on the timescale of demixing. In the LLPS limit (rapid stress relaxation/negligible viscoelastic stresses), the stress terms vanish, $\sigma^{(1)} \approx \sigma^{(2)} \approx 0$, and Eq. 1 reduces to the Cahn-Hillard equation form (*29*). Thus, LLPS is recovered as the special case of VPS in which mechanical stresses do not contribute to composition transport. In VPS, the stress is borne predominantly by the PEDOT phase, and force balance coupled to stress-diffusion drives a bicontinuous, network-like topology that can enable stress-bearing minority phase percolation before kinetic arrest, an outcome that is atypical for conventional LLPS. This mixing sequence principle is likely generalizable to other thermoreversible gel matrices along with gelatin and agarose (fig. S12), combined with an immiscible conducting polymer, provided the system develops a sufficiently large mobility/relaxation contrast during demixing.

Rheological characterizations

An essential requirement for thermoreversible neural interfaces is a controllable gel-sol transition near physiological temperature (~37°C) to enable rapid extrusion onto the scalp, followed by efficient and reversible regelation to establish conformal, stable adhesion to the skin surface, which can be experimentally validated by rheological measurements (*3*, *4*, *30*, *31*). Both NC and BC-NP systems show phase transition and thermoreversibility, whereas BC-MP (polymeric concentration between 100 and 125 w/w% aqueous PEDOT:PSS w.r.t. biogel) shows marginal gel-sol transition with high thermal hysteresis, and BC-PP (polymeric concentration more than 125 w/w%) fails to show phase transition due to its highly percolating PEDOT polymeric network (Fig. 2A and fig. S13). For the NC of 35 w/w% PEDOT:PSS, the loss tangent ($\tan\delta = G''/G'$, where G'' and G' are the loss and the storage modulus, respectively) transitions from $\tan\delta = 0.1$ at room temperature to $\tan\delta \approx 2.5$ at high temperature (50°C) and then back to $\tan\delta = 0.2$ at room temperature in 15 min (Fig. 2B, fig. S14, and note S2). Similarly, the BC-NP with 50, 75 w/w% PEDOT:PSS shows a phase transition from $\tan\delta = 0.6, 0.8$ at room temperature to $\tan\delta = 2$ at 60°C and then back to $\tan\delta = 0.9, 1.1$ at room temperature in 15 min (fig. S15). However, for BC-PP with 200, 300 w/w% PEDOT:PSS, the loss tangent reaches a maximum of $\tan\delta \approx 0.8, 0.4$, respectively, with only BC-MP of 100 w/w% barely achieving a gel-sol transition and thermoreversibility but not as efficiently as NC or BC-NP (Fig. 2C and fig. S16). With the same PEDOT polymeric concentration, the NC of 100 w/w% shows a clear phase transition of $\tan\delta \approx 2.8$, contradictory to the BC- MP of 100 w/w% (Fig. 2D and fig. S17). In NC and BC-NP, the PEDOT-rich phase remains droplet like or nonpercolated, so it cannot sustain system-spanning stress. As a result, the bulk viscoelastic response is governed primarily by the gelatin-rich matrix. Whereas at 100 w/w% BC-MP, the PEDOT-rich phase is at the onset of a system-spanning (percolated) elastic network. From this regime, elastic rigidity emerges with network connectivity, and stress relaxation becomes slower than the observation time (*27*). From this onset of percolated regime, elasticity grows steeply with connectivity, and even if the gelatin-rich phase does a gel-sol transition locally, the percolated PEDOT-rich network continues to carry load, suppressing the loss-dominated signature seen in NC. Therefore, phase transition in BC-NP occurs with low thermal hysteresis ($\Delta\tan\delta$ ~ 50% and ΔViscosity ~ 20%) after a thermal cycle (heating at 5°C/min, cooling at 5°C/min, and isothermal for 15 min), whereas BC-PP does not have a phase transition and therefore results in low thermal hysteresis ($\Delta\tan\delta$ ~ 50% and ΔViscosity ~20 to 40%). As BC-MP attains a gel-sol phase transition, the reorientation lag of the percolated network results in a high thermal hysteresis (Fig. 2E) (*32*, *33*). The emergence of a marginally percolated polymeric network imposes substantial viscoelastic constraints on thermoreversible behavior, as long-range percolation induces slow entangled chain dynamics with high relaxation times and kinetic barriers for network reorganization (which is absent for BC-PP). In the BC-MP regime, thermal hysteresis increases due to delayed disassembly of the network upon heating, reflecting the energetic cost of overcoming entangled PEDOT networks and disentangling topological constraints. However, at a highly dense percolation network of BC-PP where the polymeric network forms a quasi-permanent scaffold, the system fails to undergo a gel-sol transition. Consequently, the apparent hysteresis diminishes not due to enhanced reversibility but rather from the collapse of thermoresponsive behavior itself. Thermoreversibility is optimized when the ionic additive enhances chain mobility in the gelatin-rich phase yet does not excessively stabilize intermolecular junction zones through slow solvent-mediated interactions. In this system, the low aqueous miscibility of 1-ethyl-3-methylimidazolium bis(trifluoromethylsulfonyl)imide (EMIM-TFSI) creates a miscibility gap that produces an LLPS-derived microstructure. Such mesoscale phase separation supports rapid network rearrangement under thermal cycling, which, in turn, suppresses hysteresis and improves reversibility. In comparison, hydrophilic deep eutectic solvent (DES) (*34*, *35*) strongly solvates the PEDOT and gelatin (or agarose)/glycerol phase and reinforces an extended hydrogen bonding network, effectively increasing the activation barrier for junction dissociation/reformation (making it more stable) during heating-cooling, and therefore shows a much higher thermal hysteresis of $\Delta\tan\delta$ ~ 400% and ΔViscosity ~ 70% compared to EMIM-TFSI for NC with 35 w/w% PEDOT:PSS (Fig. 2F and fig. S18). Moreover, hydrophobic DES remains in the gel phase due to dense hydrogen bonds suppressing the chain mobility required for reorganization during heating. On the other hand, soluble 1-ethyl-3-methylimidazolium trifluoromethanesulfonate (EMIM-OTF) always remains in the solution phase with $\tan\delta > 1$ as it promotes uniform solvation (and stronger ionic screening/plasticization) to accelerate network relaxation. Along with the type of ionic liquid, increasing ionic liquid concentrations (keeping PEDOT:PSS concentration constant) (fig. S19) progressively plasticize/screen interchain associations, raising dissipation and shifting the rheological response into the viscous regime. Similarly, a combined increase in concentrations of PEDOT:PSS and ionic liquid influences the rheological (fig. S20) and tensile properties (fig. S21), even with quasistatic heating minimizing rate-dependent artifacts (fig. S22). Mechanistically, the aqueous PEDOT:PSS dispersion introduces water, strengthening gelatin (or agarose)/glycerol-mediated hydrogen bond connectivity and increasing the density of nucleated PEDOT phases, whereas the ionic liquid concurrently screens electrostatic interactions and plasticizes polymer-rich regions, enhancing chain mobility and viscous

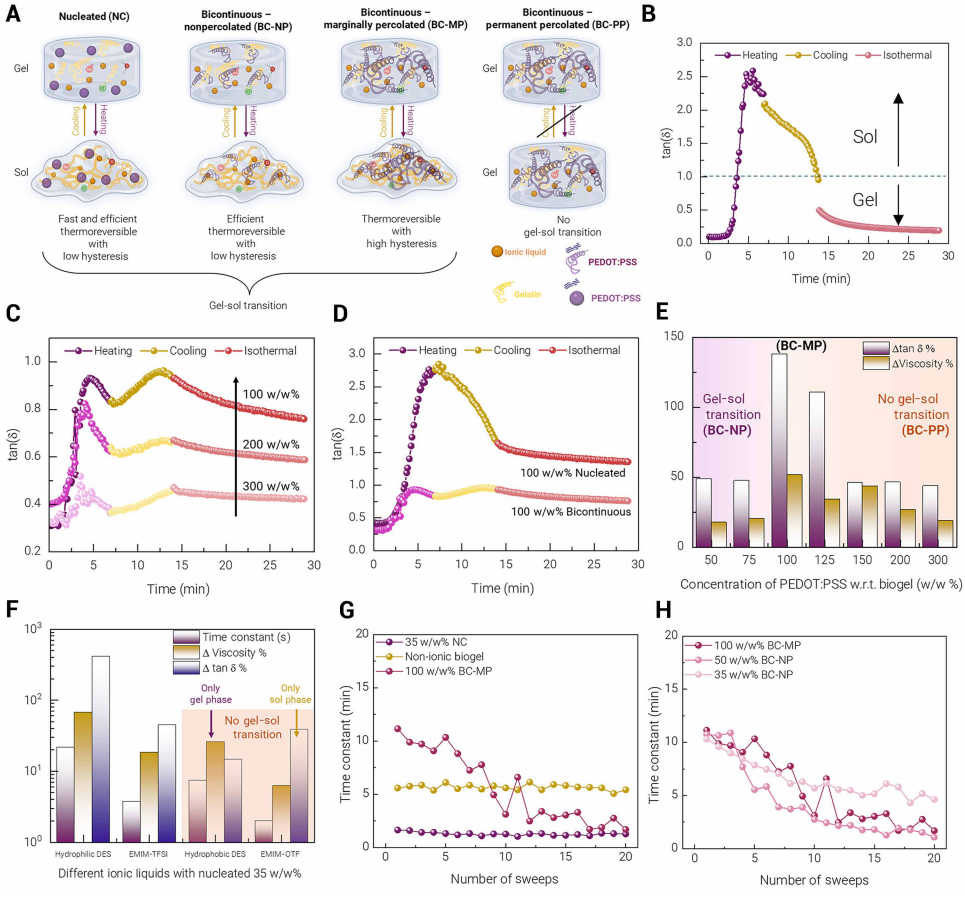

Fig. 2. Rheological performance of thermoreversible ionic biogel. (**A**) Schematic illustration comparing the efficiency of thermoreversibility of NC and BC-NP, the marginal thermoreversibility of BC-MP, and no thermoreversibility for BC-PP. The gel form of NC and BC-NP switches to sol form due to the droplet-like or nonpercolated morphology of the PEDOT network. Marginally percolated PEDOT has limited elastic connections, which marginally undergo a gel-sol transition. In contrast, permanently percolated PEDOT forms a scaffold, and therefore, the system remains in gel form after heating. (**B**) Loss tangent as a function of temperature for NC 35 w/w%. Comparison of loss tangent as a function of temperature for (**C**) 100 w/w% BC-MP and BC-PP 200, 300 w/w% and (**D**) BC-MP 100w/w% and NC 100 w/w% systems. (**E**) Comparison of rheological parameters, such as changes in loss tangent and viscosity, for different concentrations of the bicontinuous system. (**F**) Comparison of rheological parameters, such as changes in loss tangent, viscosity, and time constant of the isothermal cycle for different ionic liquids for NC 35 w/w%. Time constant of isothermal relaxation of storage modulus over 20 thermal cycles for (**G**) BC-MP, NC, and non-ionic biogels (*3*) and (**H**) BC-NP 35 w/w%, 50 w/w%, and BC-MP 100 w/w%.

dissipation. The phase-temperature maps for NC systems show a smooth, concentration-dependent evolution of viscosity with temperature rather than a sharp transition. This gradual behavior supports a morphologically stable NC state across the explored composition window, with no rheological signature indicative of spinodal decomposition or the emergence of a percolated/bicontinuous network. In contrast, for the bicontinuous system, there is a sharp decrease in viscosity from BC-PP (~15 kPa.s) to BC-NP (~300 Pa.s) at 60°C (fig. S23). This sharp change is due to the disruption of the effective entanglement of the PEDOT network, resulting in a sudden drop in viscosity rather than evolving gradually as in NC. A comparable transition is observed upon cooling but with a partial loss of thermoreversibility, consistent with kinetic trapping and slow reorganization of the PEDOT network during regelation (fig. S24). This effect is amplified when 20 thermal cycles were deployed to evaluate the time constant of each isothermal relaxation cycle for five different biogel systems (BC-MP with 100 w/w% PEDOT:PSS concentration, BC-NP with 50 and 35 w/w%, NC with 35 w/w%, and non-ionic biogel) (figs. S25 to S31). The NC shows a highly efficient thermoreversibility throughout the cycles with a time constant of ~1.6 min during the isothermal cycle of storage modulus (Fig. 2G), whereas the non-ionic biogel (*3*) shows a time constant of ~5 min. The shorter time constant for NC across cycles is due to the decrease in the correlation length and hydrogen-bonded junction zones in the gelatin matrix. Modulus recovery requires network rearrangement of gelatin matrix at hydrogen-bonded junction zones over a large correlation length, which carries a higher activation barrier and frictional penalty, yielding a longer relaxation (*27*). In NC, the ionic liquid lowers the effective barrier by screening or competing with hydrogen bonding and increasing chain mobility, while the PEDOT droplets localize stress and reduce the effective correlation length. This accelerates equilibration of the load-bearing droplet microstructure, giving the shorter, cycle-invariant time constant. The BC-MP with 100 w/w% shows a decrease in the time constant from ~12 to ~1.6 min (similar to the NC) after 20 cycles, whereas its time constant of loss modulus during the isothermal cycle sharply decreases (linearly) till the 11th cycle, and then it saturates without showing any relaxation (figs. S32 to S35). This behavior is consistent with fracture-coupled VPS (*27*): Repeated thermal

cycling accumulates internal stress and amplifies the mobility mismatch between the percolated PEDOT network and the matrix, promoting necking, strand disconnection, and incomplete rebridging of the load-bearing scaffold. As connectivity is progressively lost, the slow elastic stress relaxation modes are depleted, so the apparent relaxation time shortens toward NC/BC-NP and ultimately saturates once the response is dominated by fast dissipative/hydrodynamic rearrangements rather than recoverable network elasticity. Even with a decrease in PEDOT:PSS concentration in the BC-NP, the time constant for 35 w/w% (slowly ~0.25 min/cycle) and 50 w/w% (sharply ~0.5 min/cycle) decreases with cycles for storage modulus (Fig. 2H). Similarly, for loss modulus, the time constant decays faster with an increase in concentration: 0.6 min/cycle (100 w/w%) to 0.1 min/cycle (35 w/w%) (fig. S36).

Turbidity characterizations

In LLPS (*24*), ultraviolet-visible (UV-Vis) techniques have been effectively used to observe the increase in optical density (turbidity) and its correlation to rheological signatures of phase dynamics (*36*–*38*). Spectro-rheological framework provides a powerful, noninvasive window into thermoreversible behavior, bridging optical response and rheological state with network connectivity and its hysteresis. The NC and BC-NP exhibit classic LLPS behavior upon heating. UV-Vis temperature sweeps show a sharp onset of turbidity at the critical cloud point, which reverts upon cooling, indicating reversible, entropy-driven demixing akin to protein condensate behavior in biochemical LLPS systems (Fig. 3A) (*32*). This turbidity correlates with the nucleated PEDOT droplets, as confirmed by optical microscopy, rheology, and diffraction (Fig. 3B). In contrast, BC-MP and BC-PP show no turbidity analogous to VPS, confirming the presence of large, percolated viscoelastic networks and exhibiting pronounced UV-Vis absorbance hysteresis upon heating and cooling. For NC with 35 and 38 w/w%, the UV-Vis absorbance is observed during heating from room temperature to 60°C (Fig. 3C) and during cooling to room temperature (fig. S37). The temperature response of the NC reflects an onset of turbidity at ~37°C, where the absorbance of ~0.9 absorbance Units (a.u.) jumps to ~1.3 a.u. within a ΔT of ~5°C, reaching a highest absorbance of ~1.4 a.u. at 60°C, and then returns to an absorbance of ~1 a.u. at room temperature. Similarly, for BC-NP with 50 w/w%, the absorbance increases from ~1.2 a.u. at room temperature to ~1.75 a.u. at 60°C and returns to ~1 a.u. absorbance at room temperature (figs. S38 and S39). In contrast, for the BC-MP with 100 w/w%, the absorbance decreases from ~3 a.u. at room temperature to ~1.4 a.u. at 60°C, further decreasing to ~0.5 a.u. at room temperature (Fig. 3D

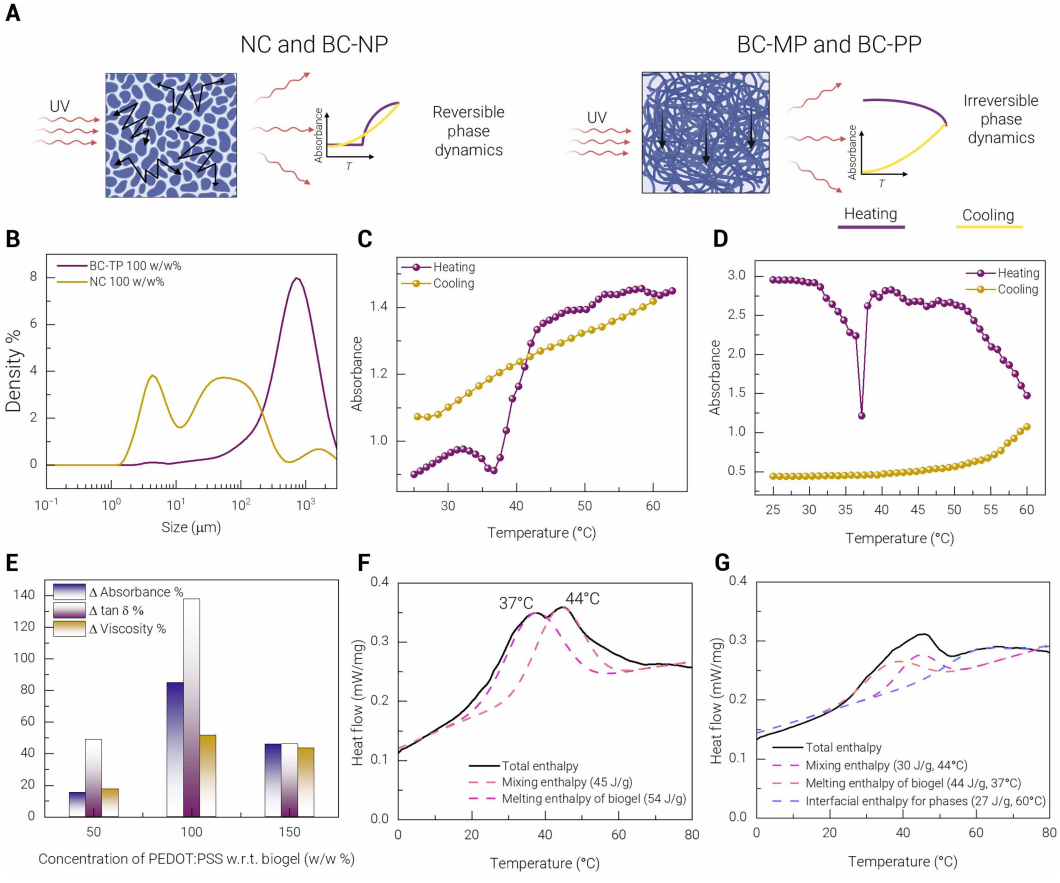

Fig. 3. Thermodynamics and kinetics of phases in ionic biogels. (**A**) Schematic illustration of phase dynamics and the onset of turbidity for NC and BC-NP (left) mimicking LLPS and no turbidity for BC-MP and BC-PP (right) mimicking VPS using UV-Vis temperature. Abs., absorbance units. (**B**) Particle size analysis of 100 w/w% BC-MP and NC 100 w/w%. Variation of UV-Vis absorbance as a function of temperature during heating and cooling of the (**C**) NC 35 w/w% system showing turbidity and (**D**) 100 w/w% BC-MP showing irreversible phase dynamics—failure of turbidity and huge thermal hysteresis. (**E**) Correlation of change in UV-Vis absorbance and rheological parameters such as loss tangent and viscosity. DSC curves of (**F**) NC 100 w/w% and (**G**) 100 w/w% BC-MP systems, showing the onset of interfacial enthalpy.

and fig. S39). The thermal hysteresis of ~85% in UV absorbance for 100 w/w% BC-MP strongly correlates with the thermal hysteresis of $\Delta\tan\delta \sim 140\%$ in rheology. Similarly, for other nucleated and bicontinuous systems, the strong correlation between thermal hysteresis and the rheological parameters (e.g., $\tan\delta$ and viscosity) reflects that optical and mechanical properties are governed by the same underlying (reversible or irreversible) phase dynamics during thermal cycling (Fig. 3E and fig. S39). Mechanistically, once the system attains the $\tan\delta \approx 1$ crossover (liquid-like regime), the BC-MP network undergoes structural rearrangement. Upon cooling, restoration of the percolated morphology requires finite reorganization time due to fracture-like disruption of the network, as also seen in decay of relaxation time constant during repeated annealing. The magnitude of UV-Vis hysteresis tracks the extent of irreversible (or slowly reversible) morphological reorganization, which also manifests as enhanced rheological hysteresis ($\tan\delta$ and viscosity) across thermal cycles. This correlation between optical hysteresis and thermo-mechanical dissipation is morphology dependent, because the energetic penalty associated with reorganizing internal interfaces scales with the interfacial area and connectivity of the PEDOT-rich phase. In NC, isolated PEDOT-rich droplets minimize surface area, and thus, the interfacial energy is not reflected in the differential scanning calorimetry (DSC) compared to its melting enthalpy due to the gelatin matrix and mixing enthalpy, whereas in BC-MP/BC-PP, the phase morphology evolves into an extended percolated PEDOT network with a large interfacial area (*39*). This structural arrangement introduces a distinct interfacial enthalpy contribution (along with mixing and melting enthalpy as in NCs) (Fig. 3F and fig. S40). Therefore, the enthalpy of bicontinuous systems arises not solely from mixing (30 J/g) or melting (44 J/g) but from interfacial energy (27 J/g) associated with the curved and sharp boundaries between the ionic and biogel phases, confirming the enthalpy-dominated thermodynamics for bicontinuous systems compared to the entropy-dominated thermodynamics for NCs (Fig. 3G).

Electrical characterizations

In phase-separated ionic biogels, the kinetics-driven phase morphology plays a pivotal role in determining charge transport pathways (*22*). NC, in which the conducting PEDOT phase forms isolated droplets within a continuous biogel matrix, exhibits predominantly ionic conductivity based on the ionic liquid. In contrast, for BC-NP, the percolated semiconducting PEDOT polymeric network spans the biogel matrix, leading to enhanced hole conductivity (Fig. 4A). With the layered structure, the hole conductivity increases markedly, making it comparable to ionic liquid-based PEDOT:PSS systems (*40*). To validate the semiconducting property of ionic biogel due to polymeric phase percolation, organic electrochemical transistors (OECTs) are deployed and characterized (Fig. 4B) (*9*, *41*–*45*). Only BC-MP and BC-PP with an extended percolated PEDOT network, as shown in previous characterizations such as rheology and turbidity, show a semiconducting nature. On the other hand, NC and BC-NP result in no OECT performance due to the lack of charge transport in the channel layer, whereas layered systems show a highly doped semiconductor with no gating. By leveraging the stimuli responsiveness in BC-MP and BC-PP, the storage modulus can be modulated by temperature, achieving subkilopascal mechanical compliance (for BC-MP) and liquid-like rheological parameters. Such physical crosslinking and stimuli responsiveness of the ionic biogel allows an active control of temperature (from 25° to 60°C). The electrical conductivity (or modulus) for BC-PP 200 w/w% increases (or decreases) from 25 S/cm (storage modulus of 22 kPa and Young's modulus of 10 kPa) to 38.5 S/cm (storage modulus of 3 kPa); similarly, the conductivity for 100 w/w% BC-MP achieves 7.7 S/cm with a storage modulus of 1.2 kPa at 60°C to enable the gel-sol transition as a highly viscous liquid (Fig. 4C). This typically breaks the flow conductivity trade-off using an active control of temperature (*15*, *16*, *46*–*50*). In passive, ambient conditions, the total conductivity and volumetric capacitance of the layered (100 w/w%) system are 140 S/cm and 8.5 F/cm^3, respectively. In comparison, for NC 100 w/w% and BC-NP 50 w/w%, the conductivity gets as low as 5.2 and 40 mS/cm, respectively, but the volumetric capacitance remains similar (~35 and 45 F/cm^3, respectively) (Fig. 4D). The high volumetric capacitance is a strong indicator of an ionic conductor, which can be confirmed by the electrochemical impedance spectra of the NC (100 w/w%) reaching ~−70° phase at low frequency (<1 kHz) to reflect an ionic behavior. In comparison, the BC-MP (100 w/w%) and BC-PP (200 w/w%) show ~0° to −10° phase, reflecting dominance of electronic conductivity over ionic (Fig. 4E and fig. S41). Similarly, in the agarose-based ionic biogel, the BC-MP route yields an impedance response that is predominantly resistive over the measured frequency range (phase angle ≈ 0°; 50 ohm, weak frequency dependence), whereas the NC route exhibits a substantially higher impedance (>1 kohm) with a pronounced capacitive signature (negative phase angle and strong frequency dispersion) (fig. S42).

The OECT with 100 w/w% BC-MP and BC-PP 300 w/w% as the active channel material exhibits a temperature-controlled normalized (by channel width) transconductance of 2.28 mS/mm (storage modulus of 750 Pa, at 100°C) and 15.5 mS/mm (storage modulus of 13 kPa, at 60°C), respectively, approaching those of traditional semiconducting hydrogels and polymers while maintaining a storage modulus of at least ~1 to 3 orders lower than the state of the art chemically crosslinked hydrogel (Fig. 4F) (*8*, *9*, *11*, *12*, *51*). Because of the gel-sol transition of 100 w/w% BC-MP, we could achieve a liquid-like $\tan\delta \approx 1$ with a normalized transconductance of 1.7 mS/mm. The high conductivity of the layered structure is reflected in the linear ohmic-like transfer characteristics with a high current of ~200 mA and poor to no gate electrostatic control, analogous to a highly doped p-type semiconductor property (with almost no gating) at −0.9 V drain bias (fig. S43) (*52*). On the other hand, for NC (200 w/w%) and BC-NP (fig. S44), the drain current and leakage gate current are of similar order without any gating or standard OECT operation. However, when the polymeric concentration reaches 100 w/w% for bicontinuous systems, the percolated PEDOT phase displays semiconducting nature symbolized with an on-current of $|I_D| \sim 1.7$ mA, improved gate electrostatic control with a low gate current of $|I_G| \sim 0.01$ mA, and a peak transconductance of 3 mS at around gate voltage of −0.17 V (Fig. 4H and fig. S45). The on-current (and peak transconductance) of the OECT increases to 19 mA (28 mS) with the increase in concentration from 100 w/w% (BC-MP) to 300 w/w% (BC-PP) (Fig. 4I and fig. S46). The figure of merit [μC^*] of the channel material (and on-off ratio of the OECT) increases from 0.8 F cm^{-1} V^{-1} s^{-1} ($I_{on}/I_{off} = 17$) to 8.4 F cm^{-1} V^{-1} s^{-1} ($I_{on}/I_{off} = 187$) with the increase in concentration from 100 to 300 w/w% (figs. S47 and S48). The mobility of the semiconducting ionic biogel increases from 0.006 to 0.043 cm^2 V^{-1} s^{-1} with the increase in concentration from 100 to 300 w/w% in the BC-MP/BC-PP, as measured using constant gate current (fig. S49) (*8*, *9*, *43*–*45*, *53*). The relatively modest hole mobility and figure of merit, when compared to state-of-the-art

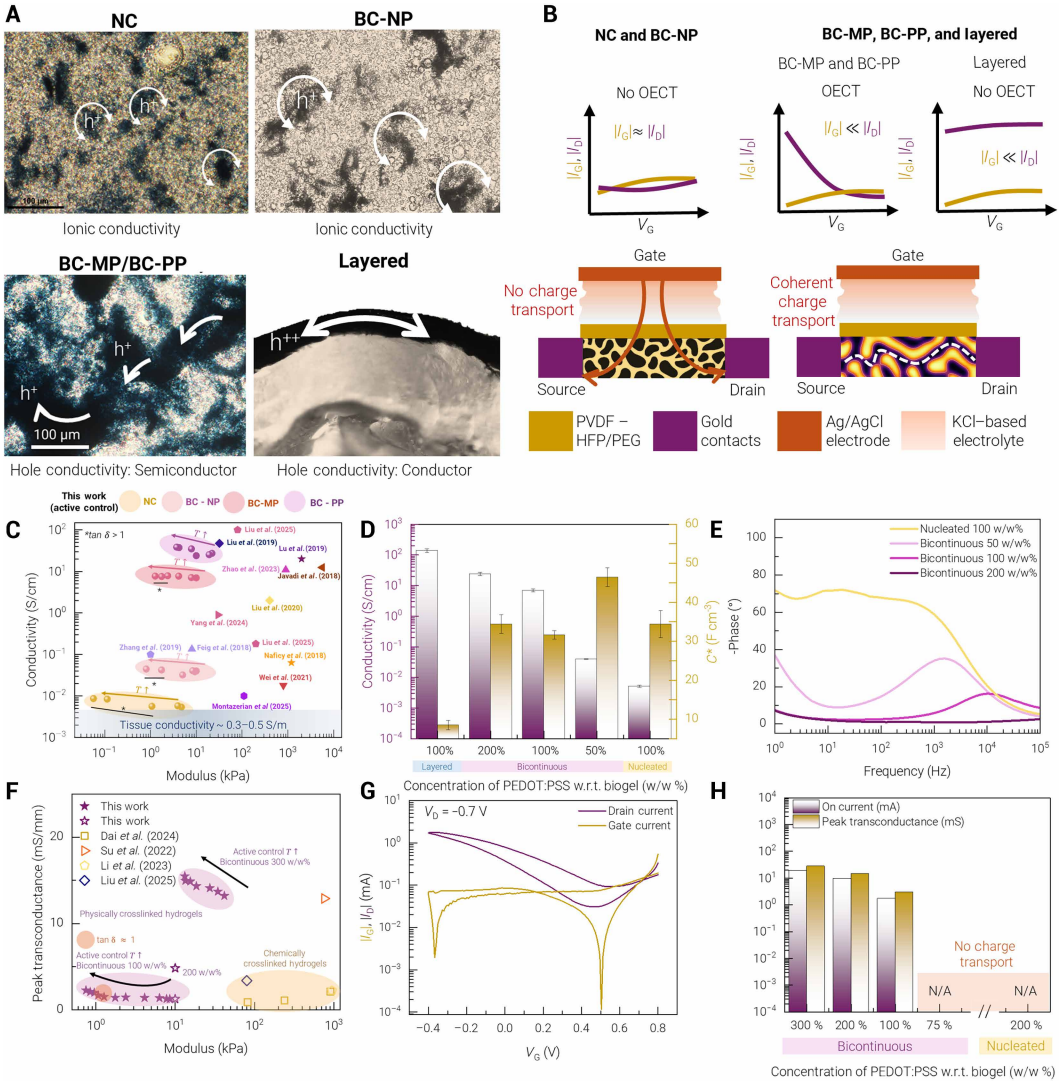

Fig. 4. Influence of phase morphology on the conductivity of ionic biogel. (**A**) Optical images to show the hole pathway through the percolated polymeric PEDOT phase in four different types of material systems. (**B**) Schematic of the OECT and the transfer characteristics for two different channel material systems: NC and BC-NP to result in no OECT and BC-MP and BC-PP to yield a standard OECT. (**C**) Benchmarking conductivity and modulus (both storage and Young's moduli marked by complete and incomplete stars) between this work and state-of-the-art conducting hydrogels (*12*, *14*, *15*, *22*, *46*–*48*, *50*). (**D**) Conductivity comparison of different types of ionic biogels—layered (100 w/w%), BC-NP (50 w/w%), BC-MP (100 w/w%), BC-PP (200 w/w%), and NC (100 w/w%). (**E**) Electrochemical impedance spectra of bicontinuous (50, 100, and 200 w/w%) and nucleated (100 w/w%) systems. (**F**) Benchmarking of normalized transconductance (by channel width) and modulus (both storage and Young's moduli marked by complete and incomplete stars) between this work and state-of-the-art semiconducting hydrogels (*8*, *9*, *51*). (**G**) Transfer characteristics of OECT with channel materials of BC-MP (100 w/w%). (**H**) Comparison of the peak transconductance and on-current of OECT with channel materials: BC-NP (75 w/w%), BC-MP (100 w/w%), BC-PP (200 and 300 w/w%), and NC (200 w/w%). N/A, not applicable.

semiconducting hydrogels (*8*, *9*, *11*, *51*), can be attributed to the fact that the investigated concentration regime represents the morphological transition point, marking the initial emergence of a percolated, electronically conductive network from an otherwise thermoreversible, ionically dominated phase. Increasing PEDOT:PSS concentration or enhancing network percolation would predictably raise mobility and improve OECT performance. However, percolation also drives the material toward a permanently arrested bicontinuous scaffold that suppresses gel-sol transitions and undermines the thermoreversibility, as shown in BC-PP (and can be further extended). The peak transconductance (and on-current) of BC-MP/BC-PP 300 and 100 w/w% increases with the increasing temperature, with a slope of 0.1 mS/K (0.07 mA/K) and 0.02 mS/K (0.01 mA/K), consistent with the thermally activated volumetric dedoping of the PEDOT network (fig. S50). The Seebeck coefficient (*54*) of NC decreases markedly from ~21 to 1.25 mV/K with the increase in concentration from 35 to 100 w/w%, as conductive PEDOT fillers suppress the Soret-induced ionic gradient and the thermogalvanic potential (note S2 and fig. S51). A similar trend is observed for the BC-MP and BC-PP, where the Seebeck coefficient decreases from 2.2 to 0.02 mV/K with the increase in concentration from 100 to 300 w/w%. Mechanistically, PEDOT network electrically shunts and screens the Soret-driven

ionic concentration gradients, thereby suppressing the associated thermogalvanic potential (*54*). This thermoelectric signature reinforces the role of the charge transport mechanism (ionic versus electronic connectivity), consistent with electrical impedance and transistor performance shown before. However, several other device-relevant properties are governed primarily by the continuous biogel matrix rather than the PEDOT-rich phase. For example, the temperature-responsive adhesion and room temperature Young's modulus (~10 kPa) of the bicontinuous system (irrespective of PEDOT: PSS concentration) can be attributed to the inherent properties of the biogel matrix (fig. S52). Similarly, the properties such as compressibility, water retention, water vapor transmission, and self-healing of NC can also be attributed to the biogel matrix (note S3 and fig. S53).

Electrophysiology characterizations

The thermoresponsive and mixed ionic-electronic conducting properties of the ionic biogel ensure stable, high-quality, long-term signal acquisition and reliable stimulation (note S4 and fig. S54) (*3*, *4*, *13*, *40*, *44*, *55*), even with different hair types or hair oils. A total of eight subjects were chosen with different hair types and oils (with subject 1 without showering throughout, resulting in accumulation of hair oils, and subject 5 after a workout) for performing different EEG experiments—open and closed eyes and mechanical (or natural) vibration over 3 days with the same electrodes containing nucleated ($n = 8$), bicontinuous ($n = 8$), and either commercial ($n = 3$) or non-ionic biogel (*3*) ($n = 5$) placed on C1, Cz, and C2 respectively—validating the reusability. In another experiment, one subject is electrically stimulated over the ulnar nerve using a wearable stimulator array over 7 days, with EEG simultaneously recorded (Fig. 5A). The skin contact impedance of BC-MP (100 w/w%) and NC (100 w/w%) remains around 1.6 kohm·cm^2 at 1 kHz (averaged over 3 days) across all the subjects, whereas the commercial gel has >100 kohm·cm^2 and the state-of-the-art non-ionic biogel performs similarly with BC-MP and NC for some subjects but has >10 kohm·cm^2 for other subjects with more dense hair (Fig. 5B and fig. S55). Even for subject 5 with accumulated sweat and salt after a workout, the ionic biogels maintained low, stable through-hair impedance (BC-MP: 2.5 kohm·cm^2, NC: 1.6 kohm·cm^2), and for subject 1 with accumulated oil and dead skin buildup, impedance stayed comparably low (NC: 0.7 kohm·cm^2; BC-MP: 1.5 kohm·cm^2) (fig. S56). Moreover, even with day 10 (for subject 6) using the same reusable electrode, the BC-MP and NC show a stable skin contact impedance of 1.7 kohm·cm^2 (from 1.2 kohm·cm^2 in day 1) and 2.4 kohm·cm^2 (1.9 kohm·cm^2 in day 1) (fig. S57). This relatively higher increase in impedance for NC is due to the accumulation of hair oil and sebum, which reduces its equivalent ionic conductivity, whereas BC-MP is more stabilized by a percolated PEDOT-rich electronic backbone. In contrast, the non-ionic biogel and a commercial gel exhibited pronounced multiday degradation, implicating loss of hydration (ions) and accumulation of salt as the dominant failure mode. The skin contact impedance across days (averaged over subjects) shows that the non-ionic biogel performs similarly to nucleated and bicontinuous, with around 2 kohm·cm^2 on day 1 but increases to 40 kohm·cm^2 on day 2 and 20 kohm·cm^2 on day 3. A similar trend is shown for the commercial electrode, with impedance increased from 6 kohm·cm^2 on day 1 to 64 kohm·cm^2 on day 3 (Fig. 5C). An increase in EEG power amplitude during the closed eyes state is observed compared to the open eyes state using both (Fig. 5D) bicontinuous and (Fig. 5E) nucleated-based electrodes over 3 days. This is also validated with the onset of alpha wave power after the 57th second, which marks the closing of the eye for subjects 3 and 4 over days 2 and 3 (fig. S58). The efficacy of the ionic biogel electrode is demonstrated through ERD in the recording of neural responses associated with motor cortex activities during mechanical or natural sensation (fig. S59) (*56*–*58*). The EEG power spectrum at C1 and Cz during sensory mechanical vibration of 50 Hz reveals an onset of ERD: a reduction in beta power amplitude on day 2 ($P < 0.01$) and day 3 ($P < 0.001$) using both nucleated (fig. S60) and bicontinuous electrodes (Fig. 5F) (*57*).

ERD has been known to occur during hand or finger movement and mechanical vibration (*56*, *58*). However, very few prior studies have correlated ERD with haptic sensations induced by transcutaneous electrical nerve stimulation (TENS) of the ulnar nerve (*59*–*62*). The perceived sensation is simultaneously recorded using a force sensor (note S5 and fig. S61), with EEG data collected using three self-balancing electrodes (with geometry optimized using simulation) (note S6 and fig. S62) at Cz, C1, and C2 through the hair. A major challenge in EEG recordings during simultaneous electrical stimulation is the introduced artifacts, particularly charging artifacts resulting from current flow through the body, which can produce high-amplitude voltages (tens of millivolts range) at the scalp and contaminate the EEG signal (in microvolts range). By positioning the ground electrode along the cervical region and ulnar nerve pathway, these artifacts are reduced from ~40 to 4 mV. The artifacts are further reduced by sequential postprocessing methods such as empirical mode decomposition (EMD) (*63*), bandpass/notch filters, and downsampling (note S7). The artifact removal is generally performed using independent component analysis (ICA) (*64*) to leverage the statistical independence of multiple channels. However, ICA's performance is restricted as the number of electrodes is only three in this work. Therefore, EMD is used to decompose the signal into several intrinsic mode functions with the first mode corresponding to the stimulation artifacts. Similar to mechanical stimulation, ERD is also observed during electrical stimulation, which is marked by a reduction of power in the alpha wave, averaged across trials for all amplitudes (Fig. 5G). Different frequencies (5 to 500 Hz) of electrical stimulation (of amplitude of 3.7 mA) are elicited to record the change of alpha power in the EEG during stimulation (Fig. 5H and note S8). This power attenuation and its spectrum across different frequencies persist on day 7 (fig. S63).

DISCUSSION

We have successfully demonstrated that precise control over polymer mixing sequences and concentrations in a PEDOT:PSS-based ionic biogel enables integrating thermoreversible mechanical adaptability with sustained electrical conductivity and semiconductivity. The nucleated and bicontinuous morphological strategies reveal distinct but complementary advantages: Nucleated morphologies provide rapid, hydration-independent thermoreversibility ideal for ionic conduction, and bicontinuous morphologies enable semiconductivity combined with thermoresponsive behavior within a carefully tuned concentration regime. By leveraging kinetic insights inspired by phase separation in biological systems, based on mixing strategy, we have achieved both nucleated PEDOT phases and transient yet stable percolated networks of PEDOT-rich phases capable of reversible transitions. This work thus establishes a robust, stimuli-responsive hydrogel platform tailored for advanced bioelectronic applications, particularly long-term, through-hair EEG interfaces requiring simultaneous

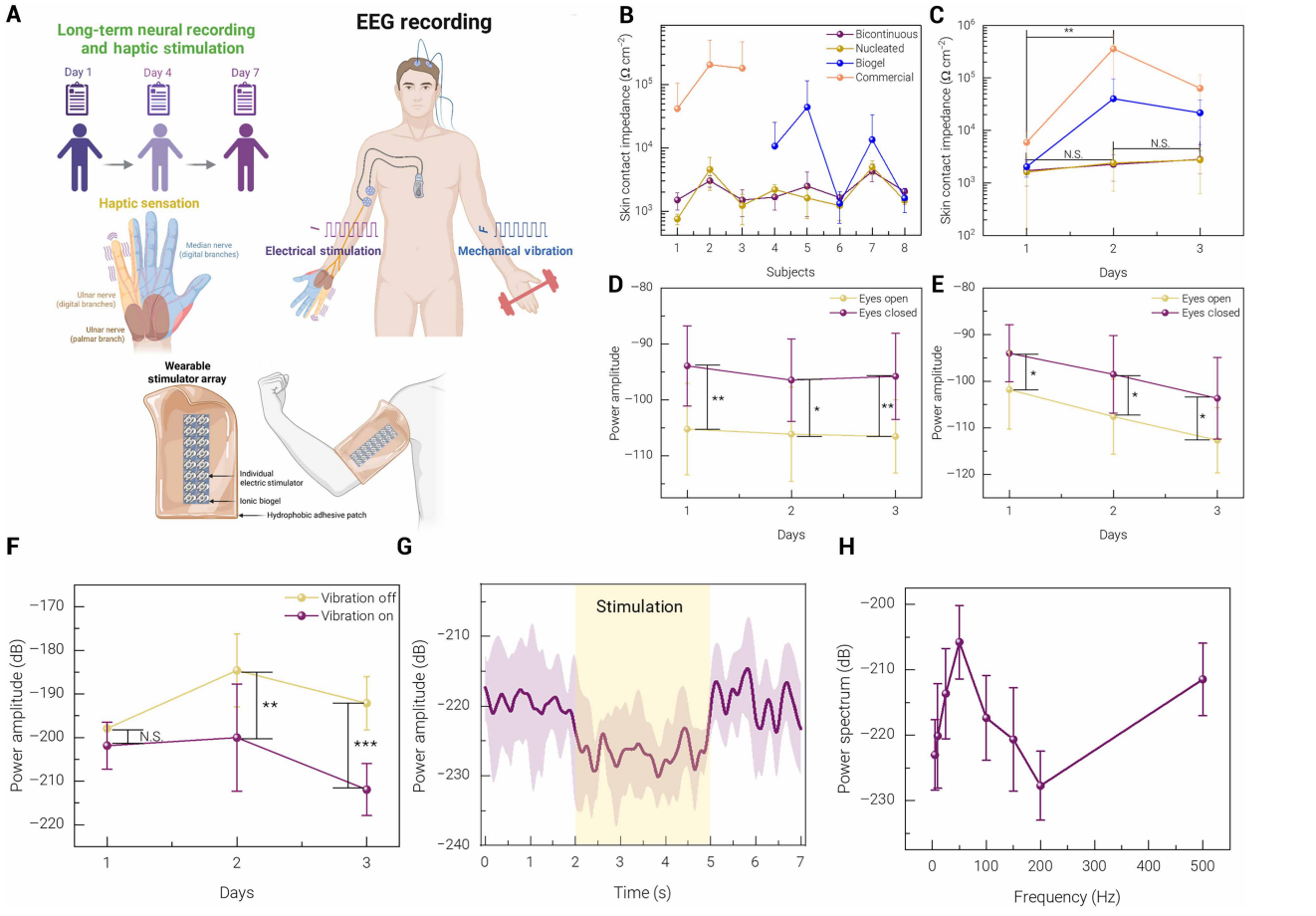

Fig. 5. Electrophysiology using ionic biogels to understand neurohaptics. (**A**) Schematic illustration of the experimental setup to analyze neural response during mechanical and electrical stimulations and schematic of the wearable electrical stimulator array placed on the arm. The skin contact impedance of BC-MP (100 w/w%), NC (100 w/w%), commercial, and non-ionic biogels (*3*) (**B**) across different human subjects (averaged over days) and (**C**) across different days (averaged over subjects). Power amplitude showing increased power in the alpha band during the eye-closing state for (**D**) bicontinuous and (**E**) NCs. (**F**) Power amplitude showing ERD during sensory mechanical vibration using bicontinuous electrodes over 3 days. (**G**) Power spectrogram of EEG during electrical stimulation at 150 Hz. (**H**) Power spectrum of EEG during haptic sensation applied at different frequencies (5 to 500 Hz) on day 1. Statistical significance is indicated as follows: N.S., not significant; $*P < 0.05$, $**P < 0.01$, and $***P < 0.001$.

mechanical adaptability and electronic robustness. The controlled phase morphology route addresses a persistent limitation of (i) supramolecular-based thermoreversible conductive hydrogel having no percolation, resulting in low conductivity, and (ii) conductive filler-based approaches with restricted gel-sol transitions. Here, we show that controlling phase morphology near the spinodal margin provides percolated morphologies while still preserving the matrix's reversible sol-gel transition. Future efforts will focus on further enhancing the semiconductive properties of the bicontinuous systems, particularly improving hole mobility and enabling coherent charge transport through precise control of polymer-dopant interactions, solvent composition, and network topology. The ionic biogel provides a platform for mixed ionic-electronic thermoelectrics, quantifying how morphology-controlled percolation and ion thermodiffusion synergistically set thermopower, power output, and stability under sustained temperature gradients. In parallel, future work will also include engineering the near room temperature sol state and toward much lower viscosity to improve processability and enable controlled thickness thin-film fabrication (e.g., spin coating), to enable high-bandwidth electrophysiology and OECT operation. In addition, strategies to minimize thermal hysteresis, such as using nucleation-promoting additives, tuning transient crosslink lifetimes, or introducing hierarchical dual-network architectures, will be pursued to ensure rapid, reproducible thermoreversible transitions without compromising electronic performance.

MATERIALS AND METHODS

Materials

Gelatin from porcine skin powder with gel strength 300 g Bloom Type A, 99% glycerol, sodium chloride (NaCl), and the ionic liquid EMIM-TFSI with a concentration of 98% (high-performance liquid chromatography) and 1-Ethyl-3-methylimidazolium trifluoromethanesulfonate (EMIM-OTF) were purchased from Sigma-Aldrich. PEDOT:PSS (Clevios™ PH 1000 PH 1000) in aqueous solution was purchased from Ossila. For PDMS, Sylgard 184 elastomer base and

its curing agent from Electron Microscopy Sciences were used at a 10:1 ratio. Ethylene glycol (EG; anhydrous, 99.8%), choline chloride (ChCl, bioreagent grade), menthol (≥99%), and thymol (≥98.5%) were all obtained from Sigma-Aldrich and used as received without further purification. KCl-based solid electrolyte and Ag/AgCl commercial disposable electrodes were bought from 3M. polyvinylidene difluoride (PVDF)–hexafluoropropylene copolymer (HFP) [with a molar mass of weight-average molecular weight (Mw) = 400,000 g mol^{-1} and number-average molecular weight (Mn) = 130,000 g mol^{-1}, respectively] was purchased from Sigma-Aldrich. Acetone was obtained from VWR Chemicals BDH Co. Ltd. Poly(ethylene glycol) (PEG) was purchased from Gelest Inc. Conductive EEG paste AC Cream was secured from Spes Medica.

Preparation of biogels

Non-ionic biogel (3). The non-ionic biogel was prepared by dissolving 0.11 g of sodium chloride in 1 ml of water. Afterward, 0.75 g of glycerol was added and mixed, followed by adding and thoroughly mixing 0.5 g of gelatin (*3*, *4*). The solution was left for 2 hours so that the gelation could occur to result in an amorphous state, and then it was heated in an oven at 80°C for 15 min. For storage or later use, the biogel was left at room temperature for around 6 hours for gelation. The biogel could be heated at any time afterward to reacquire its liquid form, showcasing its thermoreversible property (although repeated heating will change the property of this biogel, as discussed in the manuscript).

(Nucleated) ionic biogel. The (nucleated) ionic biogel was prepared by dissolving 0.11 g of sodium chloride in 2.88 ml (or 1.01 to 8.64 ml) of PEDOT:PSS in an aqueous solution, along with adding and thoroughly mixing 1 ml of ionic liquid (EMIM-TFSI, EMIM-OTF, and hydrophobic and hydrophilic DES) to obtain 100 w/w% (35 to 300 w/w%) nucleated. After 5 min, 0.75 g of glycerol was added and mixed, followed by adding and thoroughly mixing 0.5 g of gelatin (or agarose). The solution was left for 2 hours to enable gelation in an amorphous state and then heated in an oven at 80°C for 15 min (or 110°C for 15 min for agarose). For storage or later use, the resulting (nucleated) ionic biogel was left at room temperature for around 6 hours for gelation. The ionic biogel could be heated afterward to reacquire its liquid phase.

(Bicontinuous) ionic biogel. The (bicontinuous) ionic biogel was prepared by mixing 0.75 g of glycerol and 0.5 g of gelatin (or agarose) along with 0.11 g of sodium chloride and 1 ml of ionic liquid (EMIM-TFSI, EMIM-OTF, and hydrophobic and hydrophilic DES). After 5 min of gelation of gelatin-based organogel, 2.88 ml (or 1.01 to 8.64 ml) of PEDOT:PSS in an aqueous solution was mixed to obtain 100 w/w% (35 to 300 w/w%) percolated. The solution was left for 2 hours to enable gelation in an amorphous state and then heated in an oven at 80°C for 15 min (or 110°C for 15 min for agarose). For storage or later use, the resulting (bicontinuous) ionic biogel was left at room temperature for around 6 hours for gelation. The ionic biogel could be heated afterward to reacquire its liquid phase.

Layered ionic biogel. The layered ionic biogel was prepared by mixing 0.75 g of glycerol and 0.5 g of gelatin along with 0.11 g of sodium chloride and 1 ml of ionic liquid (EMIM-TFSI). After 5 min of gelation of gelatin-based organogel, 2.88 ml (or 1.01 to 8.64 ml) of PEDOT:PSS in an aqueous solution was drop casted (without mixing) to obtain the 100 w/w% layered ionic biogel. The heterogeneous material was left for 2 hours to enable gelation in an amorphous state and then heated in an oven at 80°C for 15 min. For storage or later use, the resulting layered ionic biogel was left at room temperature for around 6 hours for gelation.

Hydrophilic and hydrophobic DESs

The hydrophilic DES was prepared by mixing choline chloride (ChCl) as the hydrogen bond acceptor and EG as the hydrogen bond donor at a molar ratio of 1:2. The mixture was heated at 100°C under constant stirring at 500 rpm until a homogeneous, transparent liquid was obtained, confirming the successful formation of the DES. For the hydrophobic DES, menthol and thymol were combined at a 1:1 molar ratio and heated at 60°C with stirring at 500 rpm until a clear and uniform solution was formed.

PVDF-HFP/PEG ionic dielectric

The PVDF-HFP solution was formulated by dissolving PVDF-HFP pellets in acetone at a mass ratio of 20:3 under continuous stirring at 1000 rpm and 120°C until complete dissolution, as previously reported (*65*). Once the solution was cooled to room temperature, PEG was incorporated at concentrations of 1, 2, 4, or 6 wt % relative to the total solution volume. The PEG-modified solution was stirred at 1000 rpm for 24 hours to ensure homogeneity. Subsequently, the solution was spin-coated onto precleaned glass substrates at 1000 rpm for 30 s, followed by vacuum drying at 80°C to remove residual solvent, resulting in the formation of PEG-PVDF-HFP thin films.

OECT device fabrication

OECT devices were fabricated on polyimide substrates by thermally evaporating a bilayer of chromium (10 nm) and gold (90 nm) through a shadow mask to define the source and drain electrodes. The resulting devices had a channel length of 1 mm and a width of 3 mm. Following electrode deposition, (percolated or nucleated) semiconducting ionic biogels were heated to 80°C for 2 min and were "painted" over the channel with a tape mask to ensure uniform thickness of 50 μm and lateral dimensions as previously reported (*66*). Because of the rapid physical crosslinking property of the ionic biogel (i.e., viscosity increases rapidly under ambient conditions, therefore it becomes practically impossible to spin coat), painting was chosen over spin coating. To ensure electrical isolation and channel dimension, the semiconducting layer beyond the defined channel region was precisely trimmed using a scalpel under an optical microscope. Cured and free-standing dielectric PVDF-HFP/PEG 4% (thickness of 50 μm) was then placed on top of the semiconducting channel material (*42*). The KCl-based solid electrolyte, along with Ag/AgCl commercial electrodes, was placed vertically on top of the channel/dielectric stacking.

Methods

X-ray photoelectron spectroscopy

X-ray photoelectron spectroscopy experiments were performed using a Physical Electronics VersaProbe III instrument equipped with a monochromatic Al kα x-ray source (hν = 1486.6 eV) and a concentric hemispherical analyzer. Charge neutralization was performed using both low-energy electrons (<5 eV) and argon ions. The binding energy axis was calibrated using sputtered clean Cu (Cu 2p3/2 = 932.62 eV, Cu 3p3/2 = 75.1 eV) and Au foils (Au 4f7/2 = 83.96 eV) as in the previous report (*67*). Peaks were charge referenced to the CHx band in the carbon 1s spectrum at 284.8 eV. Measurements were made at a take-off angle of 45° with respect to the sample surface plane. This resulted in a typical sampling depth of 3 to 6 nm, with 95% of the signal originating from this depth or shallower. Quantification was done using instrumental relative sensitivity factors to account for the x-ray cross section and inelastic mean free path of the electrons. In the homogeneous samples, major elements (>5 atomic%) tend to have standard deviations of <3%, while minor elements could be substantially higher. The analysis size was ~200 μm in diameter.

UV-Vis turbidity analysis

UV-Vis spectroscopic measurements were conducted using a Lambda 950 spectrophotometer (PerkinElmer, USA) equipped with a standard photometric detector, and spectra were collected using UV WinLab software (v7.0). For the baseline correction (100% transmittance), the quartz cuvette filled with deionized water was used. Spectra were acquired over the wavelength range from 1000 to 400 nm, with a step of 1.0 nm, an acquisition time of 0.2 s per data point, and a spectral bandwidth of 2.0 nm in the UV-Vis region. In the near-infrared region, the spectral bandwidth was set to servo slit mode. The detector changes between the photomultiplier tube and the lead sulfide (PbS) detector were set to 860.8 nm, to optimize optical throughput across regions. The ionic biogel sample was placed into a short path length quartz cuvette (1-mm path length, part number: RRPG094 Pine Research, USA) to improve the transmittance of the biogel sample. To perform temperature-dependent measurements, the Versa 20 liquid cuvette holder was interfaced with a Quantum Northwest TC1 temperature controller and controlled with the T-App software (v1.52f), which enabled a uniform thermal ramp up to 60°C at a controlled rate of 0.2°C/min. The actual sample temperature was monitored in situ using an immersed type K thermocouple, with electrical readout via a USB-2001-TC (Measurement Computing, USA) module using DAQami software (v 4.2.1f0) to ensure precise thermal feedback and data acquisition fidelity.

Particle size analysis

Particle size analysis was performed using a Mastersizer 3000 (Malvern Panalytical, Netherlands) with the HydroMV dispersing cell (125 ml). Light sources of 632 nm (He-Ne laser) and 470 nm (light-emitting diode) were used for data collection. Deionized water was used as the dispersant for the testing. Data collection time was 10 s for each measurement. Five measurements were taken for each aliquot of the sample tested.

Raman spectroscopy

All Raman spectroscopy was acquired using a Horiba LabRam HR Evolution equipped with a 785-nm laser (Crystal Laser, DL-785-120-SO) coupled through a 50× Long Working Distance objective lens (numerical aperture, 0.5) with an incident laser power of 30 mW (with laser threshold test performed on the samples). The spectrometer was equipped with a 150-μm confocal hole, a 300 grooves per millimeter grating, and a Synapse BIDD Si-array detector (1024 × 512 pixels) and calibrated using the Raman response of a chip of single-crystal silicon. The temperature stage was a Linkam HFS600. Point maps were acquired after waiting a minimum of 3 min after the temperature stage reached the desired set point temperature.

Fourier transform infrared

Infrared spectra were collected in attenuated total reflection (ATR) geometry on a Bruker Vertex 70 spectrometer equipped with a liquid nitrogen–cooled mid-band mercury cadmium telluride detector and a Harrick Diamax ATR accessory with a heatable solid sampling adapter. A background (bare crystal) and a sample spectrum were collected after 10 min of equilibration at each temperature. A total of 400 scans were averaged at 4 cm^{-1} resolution, with the absorbance calculated by referencing to the clean bare diamond ATR crystal.

Atomic force microscopy

The peak force tapping quantitative nanomechanical mapping experiments were performed in air on a BiosScope Resolve (Bruker). RTESPA150 (Bruker) probes were used with a nominal tip radius of 5 nm and a spring constant of 6 N/m. Scans over 20 μm by 2 μm were performed with a probe vibration frequency of 2 kHz, a peak force amplitude of 150 nm, 512 samples per line, and a scan rate of 0.35 Hz. Images were analyzed with NanoScope Analysis v.3.

Wide-angle x-ray scattering

The wide-angle x-ray scattering experiments were performed on a laboratory beamline (Xeuss 2.0 HR, Xenocs, France) using a GeniX3D microfocus sealed tube (copper) beam source with an x-ray wavelength of 1.54 Å and power settings of 50 kV and 0.6 mA. A Dectris Pilatus3 R200K detector was used with a sample-to-detector distance of ~0.15 m. The scattering experiments were collected at 27°, 40°, 50°, 60°, and again at 27°C using silicon scatterless slits for collimation (1.2 and 0.8 mm). The two-dimensional (2D) images were integrated using "X-ray Scattering Analysis and Calculation Tool" (XSACT version 2.6) software from Xenocs to convert 2D images into 1D scattering data of scattering intensity I(q) (in arbitrary units) versus 2θ. Each image was produced by collecting and summing three vertical images (300 s each with line eraser mode). Line eraser mode is a function designed by the manufacturer to allow images to be overlapped to correct for nonsensitive areas in the summed 2D images caused by the detector (built from multiple sensor modules tied together).

Microcomputed tomography imaging

High-resolution microcomputed tomography (μCT) was used to nondestructively visualize and quantify the internal microarchitecture of the ionic biogels, enabling differentiation between nucleated and bicontinuous morphologies. Biogel samples were prepared in cylindrical polyethylene tubes to prevent dehydration and movement during scanning. μCT images were obtained on a Zeiss Xradia 620 (Germany). The voltage used was 70 kV, and the power was 8.5 W with 3001 projections and a 1-s exposure. The low energy x-ray filter LE1 filter was used. The reconstruction was obtained from the Scout and Scan Software (Zeiss, Germany). The voxel size of the image was 1.3 μm.

Biocompatibility test

Hydrogel samples were cut into circular films with a 10-mm diameter and added to phosphate-buffered saline to prepare hydrogel extracts, and 1.0 ml of the extract was put into a 24-well plate for UV irradiation. For each well containing hydrogel extract, 2×10^4 MCF-10A was added, and the proliferation medium was supplemented to 1.0 ml. For the wells without material as the control group, 2×10^4 MCF-10A was also added, and the proliferation medium was supplemented to 1.0 ml. The 24-well plate containing MCF-10A and the extract was incubated in a cell culture incubator, and 200 μl of proliferation medium was added to each well every 2 days. The proliferation of MCF-10A on the hydrogel extract on days 1 and 2 after coculture was determined using MTT. After adding the fluorescein diacetate, the staining results were observed using a fluorescence microscope.

Seebeck coefficient measurement

Seebeck coefficient measurement was performed using a custom-designed setup (fig. S64). Two copper blocks, connected to circulating water as heater/chiller units, were used to generate a temperature gradient across the samples in a planar configuration. One of the copper blocks maintained a continuous flow of water at a temperature of 9°C, whereas the other block was subjected to incremental cooling and heating and maintained at varying temperatures through a chiller from 0° to 30°C. Two thermocouples were attached to the edge of the samples on two sides to monitor real-time temperature changes. The voltage change was recorded after a stable temperature was reached.

DSC measurement

The thermal properties were measured by DSC (Netzsch DSC 214, Germany) under an Ar atmosphere with a heating rate of 2°C/min.

Mechanical testing

General procedures. All mechanical and adhesive testing was conducted on an Instron J5966 testing frame (Instron, Binghamton, NY, USA) with a 1-kN load cell and using Bluehill Universal mechanical testing software (Instron).

Compression testing. Compression testing between parallel plates (Instron) was carried out on hydrogel specimens with a diameter of 8 mm and a thickness of 1 mm to 90% strain at a strain rate of 1.3 mm/min. Initial modulus and peak stress at 90% strain were calculated from the stress profile over the initial 10% strain and the maximum stress value, respectively.

Tensile testing. Tensile testing was carried out using pneumatic grips (Instron) on hydrogel samples (length × width × thickness: 3 cm by 1 cm by 1 mm) at a strain rate of 50 mm/min. Initial tensile modulus, peak stress, and peak strain were calculated from the stress profile over the initial 10% of strain and the maximum stress and strain values, respectively.

Adhesive testing. Lap shear adhesive testing was carried out using pneumatic tensile grips. Strips of porcine tissue (1-cm width) were adhered in a lap configuration with an adhesive area of 1 cm^2 and placed within the tensile grips (with the adhered region facing outside of the gripped area). The tensile force was then applied at a rate of 5 mm/min until adhesive failure, with the maximum adhesive force recorded. The 90° adhesive peel testing was carried out by first gluing a porcine tissue strip (1-cm width) to a flat acrylic plate, which was then attached to the bottom compression plate of the mechanical testing frame using vice grips. Another strip of porcine tissue was adhered to this first piece using the appropriate hydrogel adhesive to create an adhesive area of 1 cm^2. The other, free end of the second strip was then gripped by the top pneumatic grip of the testing frame, after which a tensile force was applied to the top to achieve the 90° peel, with adhesive force measured as above.

Rheological testing

General procedures. All rheological testing was conducted on a DHR-2 rheometer (TA Instruments, New Castle, DE, USA) using TRIOS software (TA Instruments) in a 20-mm parallel plate configuration (sandblasted plate faces) with a Peltier plate to control the temperature. Hydrogel samples with a diameter of 20 mm and a height of 1 mm were used at 25°C unless stated otherwise.

Shear sweep. Shear sweeps were first conducted to establish the linear response region from 0.01 to 1000% strain at a frequency of 1 Hz.

Frequency sweep. Frequency sweeps were conducted from 0.1 to 100 Hz within the linear response region (0.05% strain).

Temperature sweep. Temperature sweeps were conducted in three phases: (i) an initial ramp from 25° to 60°C at a rate of 5°C/min, (ii) a cooling ramp from 60° to 25°C at a rate of 5°C/min, and (iii) a recovery interval at 25°C for 900 s (all at 1 Hz and 0.05% strain).

Cyclical recovery test. The above three phases were repeated over 20 successive cycles.

Temperature adhesion test. Tensile adhesion tests were performed by placing the ionic biogel between two skin phantoms, which were strongly adhered to the aluminum plates at both ends. The ionic biogel, along with the skin, was preheated to different temperatures from 30° to 60°C and returned to room temperature (25°C). After a holding time of 5 min at room temperature, the axial force and displacement were noted at each cycle to evaluate the temperature-dependent interfacial adhesion stiffness and toughness.

Stimulation procedure

A 26-year-old male human subject participated in the stimulation experiment. During the experiment, the subject was comfortably seated in a chair. The electrical stimuli were delivered via a set of 2 × 8 gel-based electrodes (Fig. 5A). Each electrode with a diameter of 1 cm was replaced with the reported ionic biogel to enhance conductivity. The electrodes were positioned along the medial portion of the right upper arm, just beneath the short head of the biceps brachii, targeting the area near the median and ulnar nerves. This placement aligned with the way that extended from the center of the armpit to the inner side of the elbow (medial epicondyle of the humerus), ensuring placement over the nerve pathways located below the skin. To deliver the electrical stimuli via a specific pair of electrodes (Fig. 5A), a custom-built MATLAB interface to control a switch matrix (Agilent Technologies, Santa Clara, CA) for electrode pair selection was used. The MATLAB interface was also used to configure the stimulation parameters of the stimulator (STG4008, Multichannel Systems, Reutlingen, Germany). Specifically, single biphasic rectangular pulses were delivered to selected electrodes with a pulse width of 200 μs and a stimulation frequency of 150 Hz. To indicate the force evoked by stimulation, the subject's right hand was placed on a force load cell (LCM201-100 N, Newark Electronics, Chicago, IL) with a sampling frequency of 1000 Hz, allowing the subject to apply varying levels of pressure with the index finger in response to the force evoked by stimulation as in the previous report (*59*). A grid search was initially performed to identify a pair of electrodes that could effectively induce flexion in at least one finger while minimizing wrist movement and avoiding any discomfort. Once identified, this electrode pair was used for subsequent experiments. Multiple 3-s stimulation trials were conducted, with the pulse amplitude gradually increased until the subject reported discomfort. The measured forces during the plateau period were averaged to indicate the force evoked by stimulation. The evaluation of the long-term usability of the reported ionic biogel involved a series of experiments over the span of 1 week, specifically on days 1, 2, 4, and 7. The human subject study was approved by The Pennsylvania State University (protocol numbers STUDY00009245 and STUDY00021035), with informed consent obtained from the volunteer.

Image processing for phase morphology

Raw optical micrographs were converted from RGB color space to the CIE Lab* color space, and the luminance channel (L*) was extracted for subsequent analysis. This transformation isolated intensity information from chromatic variations, providing optimal contrast between the PEDOT:PSS-rich and gelatin-rich phases. When necessary, contrast enhancement was performed using contrast limited adaptive histogram equalization, dividing the image into tiles and applying histogram equalization locally with amplitude limiting to prevent noise amplification. A clip limit of 0.01 to 0.03 was used depending on the initial image contrast. Pixel calibration was performed using scale bars embedded in each micrograph, yielding typical pixel sizes of 2 to 10 μm/pixel depending on optical magnification. Segmentation of the PEDOT:PSS-rich phase was performed using percentile-based intensity thresholding. Percentile thresholding enabled the selective isolation of the darkest image regions corresponding to the conducting PEDOT phase. A threshold was set at the pth percentile of the grayscale intensity histogram, where $p = 15$ to 25 was selected on the basis of the specific morphology being analyzed. Pixels with intensities below this threshold were classified as belonging to the

PEDOT:PSS-rich phase. Small, isolated noise features were removed by eliminating connected regions smaller than a minimum area threshold (typically 50 pixels). Domain identification was performed using connected component analysis with 8-connectivity, where pixels sharing either edges or corners were considered connected. Critically, all connected pixels were treated as belonging to a single domain, preserving the inherent connectivity of bicontinuous phase-separated structures. This approach ensured that interconnected regions characteristic of VPS were analyzed as unified domains rather than being artificially partitioned. Each distinct connected region in the binary mask was assigned a unique label, enabling individual domain characterization while maintaining the topological integrity of the phase-separated morphology. To focus quantitative analysis on morphologically major features and exclude noise artifacts, the N largest domains were retained (typically $N = 50$). Selection was performed by ranking all identified domains according to their projected area and retaining the top N domains. For bicontinuous morphologies where domains may span large portions of the field of view, this selection criterion ensures that the analysis captures the dominant phase-separated structures. For each identified domain, the following morphometric parameters were computed. The projected area (A) is the total number of pixels within the domain multiplied by the squared pixel size. The perimeter (P) is the length of the domain boundary, computed using 8-connectivity chain code representation. The equivalent diameter (d_{eq}) is defined as the diameter of a circle with equivalent area: $d_{eq} = (4A/\pi)^{1/2}$. The two-point correlation function $S_2(r)$ quantifies the probability that two points separated by distance r both reside within the PEDOT:PSS-rich phase. The correlation length (ξ) was defined as the distance at which $S_2(r)$ decays to $1/e$ of its zero-distance value, providing a characteristic length scale of the phase-separated structure.

Electrochemical measurements

Electrochemical impedance spectroscopy. Electrochemical impedance spectroscopy was performed using a MetroOhm Autolab Potentiostat electrochemical workstation, with thin ionic biogel on gold/polyimide substrates serving as the working electrodes. A silver/silver chloride (Ag/AgCl) electrode served as the reference, with a platinum electrode as the counter electrode. The three-electrode setup was submerged in a solution consisting of potassium ferricyanide(III) (0.01 M) and potassium hexacyanoferrate(II) trihydrate (0.01 M), over a frequency range spanning from 100 kHz to 1 Hz, using a sinusoidal perturbation of 10 mV superimposed on a 0.1-V dc bias. The resulting impedance spectra were analyzed using the MATLAB 2024b software. Capacitance and resistance values were extracted through equivalent circuit fitting by using a simplified Randles model for nucleated and a dual-Randles model for bicontinuous systems, which were further normalized by the geometric dimensions.

Charge injection capacity. The charge injection capacity (CIC) is a critical parameter that ensures the safety of electrodes during stimulation. It is defined as the maximum charge density that an electrode can inject without exceeding the water electrolysis threshold. Exceeding these thresholds can result in electrode damage, the generation of toxic by-products, or tissue damage. Safe stimulation relies on maintaining the maximum cathodal voltage (E_{mc}) within the electrochemical water window, typically between −0.6 and 0.8 V, as previously reported (*68*).

Voltage-transient analysis: The CIC is derived from voltage transients during a biphasic current pulse. The cathodal and anodal pulse widths (t_c and t_a) and respective currents (i_c and i_a) determine the injected charge

$$Q_{inj} = \int_0^{t_c} i_c(t)dt + \int_0^{t_a} i_a(t)dt \tag{2}$$

The maximum cathodal excursion potential (E_{mc}) is measured immediately after the pulse and corrected for access voltage (V_a) due to series resistance

$$E_{mc} = V_{transient} - V_a \tag{3}$$

Charge injection limits: The CIC is the maximum charge density that can be injected without the onset of water reduction (cathodal limit) or oxidation (anodal limit)

$$CIC = \frac{Q_{inj}}{A_{eff}} \tag{4}$$

where A_{eff} is the geometric surface area of the electrode.

Electrochemical window constraints: Safety requirements indicate $E_{mc} > -0.6$ V and $E_{ma} < 0.8$ V. The frequency (f) of stimulation is inversely related to the total period (T) of the waveform, which includes both the cathodal (t_c) and anodal (t_a) pulse widths, as well as the interphase delay (t_{ip})

$$f = \frac{1}{T} \tag{5}$$

where $T = t_c + t_a + t_{ip}$. Here, cathodal and anodal pulse widths are the same $t_c = t_a = t$, and interphase delay $t_{ip} = 10$ ms is kept constant. Therefore, a shorter pulse width signifies a higher frequency with

$$f = \frac{1}{2t + 10\ \text{ms}} \tag{6}$$

OECT measurements

Transfer and output curves. All transfer and output characteristics for OECT measurements were performed using a Keysight B1500A parameter analyzer under ambient conditions (and at higher temperatures for studying temperature-dependent properties). The voltage sweep rate was maintained at 8 mV/s unless stated otherwise.

Bandwidth measurements. High-speed, drain-current measurements (with a bias $V_D = -0.7$ V) were performed using a PZ2100A high-density precision source measurement unit (SMU) mainframe with PZ2121A high-speed SMUs, whereas gate voltages were applied from a RIGOL DG4102 waveform generator.

Mobility measurements. The charge carrier mobility (μ) of the biogel semiconductor during OECT operation was determined by evaluating the hole transit time (τ_h), following previously established protocols (*8*, *9*, *42*). In this method, constant gate currents (I_g) were applied to the device while maintaining a fixed drain-source bias ($V_D = -0.1$ V) with a gate compliance of $V_G = 0.6$ V. The resulting transient response of the drain channel current was recorded to extract τ_h using

$$\frac{\partial I_D}{\partial t} = -\frac{I_G}{\tau_h} \tag{7}$$

The mobility was then calculated using the relation

$$\mu = \frac{L^2}{\tau_h \times V_D} \tag{8}$$

where L denotes the channel length.

Electrical measurements

Electrical impedance. Electrical impedance spectra were taken using the Hioki IM 3536-01 LCR Meter under ambient conditions (or at higher temperatures for studying temperature-dependent properties). The stability tests of the bicontinuous and nucleated ionic biogels in the sandwich configuration were performed over 21 days, with the electrical impedance spectra measured each day under ambient conditions.

Electrophysiology measurements. The electromyogram and EEG signals were measured using the BioAmp data acquisition system (AD Instruments).

Two-terminal measurements. Two-terminal I-V measurements were performed using a Keithley 2401 source meter.

Supplementary Materials

This PDF file includes:

Supplementary Texts S1 to S8
Figs. S1 to S64
Table S1

REFERENCES

1. W. Park, L. Kim, T. Ball, S. F. Atashzar, Editorial: NeuroHaptics: From human touch to neuroscience. *Front. Neurosci.* **16**, 964014 (2022).
2. H. Alsuradi, W. Park, M. Eid, EEG-based neurohaptics research: A literature review. *IEEE Access* **8**, 49313–49328 (2020).
3. C. Wang, H. Wang, B. Wang, H. Miyata, Y. Wang, M. O. G. Nayeem, J. J. Kim, S. Lee, T. Yokota, H. Onodera, T. Someya, On-skin paintable biogel for long-term high-fidelity electroencephalogram recording. *Sci. Adv.* **8**, eabo1396 (2022).
4. L. Lan, J. Ping, H. Li, C. Wang, G. Li, J. Song, Y. Ying, Skin-inspired all-natural biogel for bioadhesive interface. *Adv. Mater.* **36**, e2401151 (2024).
5. A. C. Beijora, A. P. Back, A. R. Fréz, M. R. B. Azevedo, G. R. F. Bertolini, Peripheral electrical stimulation on neuroplasticity and motor function in stroke patients: A systematic review and meta-analysis. *Neurol. Res.* **45**, 1111–1126 (2023).
6. R. L. J. Meesen, K. Cuypers, J. C. Rothwell, S. P. Swinnen, O. Levin, The effect of long-term TENS on persistent neuroplastic changes in the human cerebral cortex. *Hum. Brain Mapp.* **32**, 872–882 (2011).
7. S. L. Norman, J. R. Wolpaw, D. J. Reinkensmeyer, Targeting neuroplasticity to improve motor recovery after stroke: An artificial neural network model. *Brain Commun.* **4**, fcac264 (2022).
8. Y. Dai, S. Wai, P. Li, N. Shan, Z. Cao, Y. Li, Y. Wang, Y. Liu, W. Liu, K. Tang, Y. Liu, M. Hua, S. Li, N. Li, S. Chatterji, H. C. Fry, S. Lee, C. Zhang, M. Weires, S. Sutyak, J. Shi, C. Zhu, J. Xu, X. Gu, B. Tian, S. Wang, Soft hydrogel semiconductors with augmented biointeractive functions. *Science* **386**, 431–439 (2024).
9. N. Li, Y. Li, Z. Cheng, Y. Liu, Y. Dai, S. Kang, S. Li, N. Shan, S. Wai, A. Ziaja, Y. Wang, J. Strzalka, W. Liu, C. Zhang, X. Gu, J. A. Hubbell, B. Tian, S. Wang, Bioadhesive polymer semiconductors and transistors for intimate biointerfaces. *Science* **381**, 686–693 (2023).
10. J. Chong, C. Sung, K. S. Nam, T. Kang, H. Kim, H. Lee, H. Park, S. Park, J. Kang, Highly conductive tissue-like hydrogel interface through template-directed assembly. *Nat. Commun.* **14**, 2206 (2023).
11. P. Li, W. Sun, J. Li, J.-P. Chen, X. Wang, Z. Mei, G. Jin, Y. Lei, R. Xin, M. Yang, J. Xu, X. Pan, C. Song, X.-Y. Deng, X. Lei, K. Liu, X. Wang, Y. Zheng, J. Zhu, S. Lv, Z. Zhang, X. Dai, T. Lei, N-type semiconducting hydrogel. *Science* **384**, 557–563 (2024).
12. S. Zhang, Y. Chen, H. Liu, Z. Wang, H. Ling, C. Wang, J. Ni, B. Çelebi-Saltik, X. Wang, X. Meng, H.-J. Kim, A. Baidya, S. Ahadian, N. Ashammakhi, M. R. Dokmeci, J. Travas-Sejdic, A. Khademhosseini, Room-temperature-formed PEDOT:PSS hydrogels enable injectable, soft, and healable organic bioelectronics. *Adv. Mater.* **32**, e1904752 (2020).
13. H. Yuk, B. Lu, X. Zhao, Hydrogel bioelectronics. *Chem. Soc. Rev.* **48**, 1642–1667 (2019).
14. H. Montazerian, E. Davoodi, C. Wang, F. Lorestani, J. Li, R. Haghniaz, R. R. Sampath, N. Mohaghegh, S. Khosravi, F. Zehtabi, Y. Zhao, N. Hosseinzadeh, T. Liu, T. K. Hsiai, A. H. Najafabadi, R. Langer, D. G. Anderson, P. S. Weiss, A. Khademhosseini, W. Gao, Boosting hydrogel conductivity via water-dispersible conducting polymers for injectable bioelectronics. *Nat. Commun.* **16**, 3755 (2025).
15. B. Lu, H. Yuk, S. Lin, N. Jian, K. Qu, J. Xu, X. Zhao, Pure PEDOT:PSS hydrogels. *Nat. Commun.* **10**, 1043 (2019).
16. V. R. Feig, H. Tran, M. Lee, Z. Bao, Mechanically tunable conductive interpenetrating network hydrogels that mimic the elastic moduli of biological tissue. *Nat. Commun.* **9**, 2740 (2018).
17. J. Deng, J. Wu, X. Chen, T. L. Sarrafian, C. E. Varela, W. Whyte, C. F. Guo, E. T. Roche, L. G. Griffiths, H. Yuk, C. S. Nabzdyk, X. Zhao, A bioadhesive pacing lead for atraumatic cardiac monitoring and stimulation in rodent and porcine models. *Sci. Transl. Med.* **16**, eado9003 (2024).
18. V. S. Damani, X. Xie, R. E. Daso, K. Suman, M. Ghasemi, W. Xie, R. Wu, Y. Wu, C. L. Chao, J. E. Alberto, C. M. Lorch, A.-N. Yang, D. M. Nguyen, T. Shrestha, K. Otero, C.-Y. Lo, D. J. Pochan, E. D. Gomez, J. Rivnay, L. V. Kayser, Thermo-reversible gelation of self-assembled conducting polymer colloids. *Nat. Commun.* **16**, 10879 (2025).
19. E. Trepka, L. Cooper, K. Brinson, S. Thompson, M. G. Malinao, N. J. Rommelfanger, P. Fordyce, G. Hong, Acoustic printing of conductive polymers. *Proc. Natl. Acad. Sci. U.S.A.* **122**, e2509652122 (2025).
20. Y. Yang, Y. Ren, W. Song, B. Yu, H. Liu, Rational design in functional hydrogels towards biotherapeutics. *Mater. Des.* **223**, 111086 (2022).
21. X. Jing, X.-Y. Wang, H.-Y. Mi, L.-S. Turng, Stretchable gelatin/silver nanowires composite hydrogels for detecting human motion. *Mater. Lett.* **237**, 53–56 (2019).
22. T. Zhou, H. Yuk, F. Hu, J. Wu, F. Tian, H. Roh, Z. Shen, G. Gu, J. Xu, B. Lu, X. Zhao, 3D printable high-performance conducting polymer hydrogel for all-hydrogel bioelectronic interfaces. *Nat. Mater.* **22**, 895–902 (2023).
23. C. P. Brangwynne, C. R. Eckmann, D. S. Courson, A. Rybarska, C. Hoege, J. Gharakhani, F. Jülicher, A. A. Hyman, Germline P granules are liquid droplets that localize by controlled dissolution/condensation. *Science* **324**, 1729–1732 (2009).
24. J. Liu, X. Liu, T. Zhang, J. Huang, B. Z. Tang, Y. Chau, Metastable biological matter in liquid phase separation. *Appl. Res.* **3**, e202300071 (2024).
25. L. Li, Z. Hou, Theoretical modelling of liquid–liquid phase separation: From particle-based to field-based simulation. *Biophys. Rep.* **8**, 55–67 (2022).
26. C. Duan, R. Wang, A unified description of salt effects on the liquid–liquid phase separation of proteins. *ACS Cent. Sci.* **10**, 460–468 (2024).
27. H. Tanaka, Viscoelastic phase separation. *J. Phys. Condens. Matter* **12**, R207–R264 (2000).
28. H. Tanaka, Viscoelastic model of phase separation. *Phys. Rev. E* **56**, 4451 (1997).
29. H. Tanaka, Viscoelastic phase separation in biological cells. *Commun. Phys.* **5**, 167 (2022).
30. T. Hirose, K. Ninomiya, S. Nakagawa, T. Yamazaki, A guide to membraneless organelles and their various roles in gene regulation. *Nat. Rev. Mol. Cell Biol.* **24**, 288–304 (2023).
31. T. Kopač, Mathematical model for characterization of temperature-responsive polymers: A study on the rheological behavior of gelatin and poly(N-isopropylacrylamide). *Polym. Test.* **133**, 108402 (2024).
32. E. Bouchbinder, J. S. Langer, Nonequilibrium thermodynamics and glassy rheology. *Soft Matter* **9**, 8786–8791 (2013).
33. R. Malik, D. Burch, M. Bazant, G. Ceder, Particle size dependence of the ionic diffusivity. *Nano Lett.* **10**, 4123–4127 (2010).
34. E. L. Smith, A. P. Abbott, K. S. Ryder, Deep eutectic solvents (DESs) and their applications. *Chem. Rev.* **114**, 11060–11082 (2014).
35. J.-Y. Yang, A. Kumar, M. O. Shaikh, S.-H. Huang, Y.-N. Chou, C.-C. Yang, C.-K. Hsu, L.-C. Kuo, C.-H. Chuang, Biocompatible, antibacterial, and stable deep eutectic solvent-based ionic gel multimodal sensors for healthcare applications. *ACS Appl. Mater. Interfaces* **15**, 55244–55257 (2023).
36. S. Ambadipudi, J. Biernat, D. Riedel, E. Mandelkow, M. Zweckstetter, Liquid–liquid phase separation of the microtubule-binding repeats of the Alzheimer-related protein Tau. *Nat. Commun.* **8**, 275 (2017).
37. M. Cui, X. Wang, B. An, C. Zhang, X. Gui, K. Li, Y. Li, P. Ge, J. Zhang, C. Liu, C. Zhong, Exploiting mammalian low-complexity domains for liquid-liquid phase separation–driven underwater adhesive coatings. *Sci. Adv.* **5**, eaax3155 (2019).
38. A. D. Malay, T. Suzuki, T. Katashima, N. Kono, K. Arakawa, K. Numata, Spider silk self-assembly via modular liquid-liquid phase separation and nanofibrillation. *Sci. Adv.* **6**, eabb6030 (2020).
39. M. Z. Bazant, Theory of chemical kinetics and charge transfer based on nonequilibrium thermodynamics. *Acc. Chem. Res.* **46**, 1144–1160 (2013).
40. Y. Wang, C. Zhu, R. Pfattner, H. Yan, L. Jin, S. Chen, F. Molina-Lopez, F. Lissel, J. Liu, N. I. Rabiah, Z. Chen, J. W. Chung, C. Linder, M. F. Toney, B. Murmann, Z. Bao, A highly stretchable, transparent, and conductive polymer. *Sci. Adv.* **3**, e1602076 (2017).
41. L. Lu, X. Liu, P. Gu, Z. Hu, X. Liang, Z. Deng, Z. Sun, X. Zhang, X. Yang, J. Yang, G. Zu, J. Huang, Stretchable all-gel organic electrochemical transistors. *Nat. Commun.* **16**, 3831 (2025).
42. C. G. Bischak, L. Q. Flagg, D. S. Ginger, Ion exchange gels allow organic electrochemical transistor operation with hydrophobic polymers in aqueous solution. *Adv. Mater.* **32**, e2002610 (2020).
43. J. Rivnay, S. Inal, A. Salleo, R. M. Owens, M. Berggren, G. G. Malliaras, Organic electrochemical transistors. *Nat. Rev. Mater.* **3**, 17086 (2018).

44. J. Rivnay, S. Inal, B. A. Collins, M. Sessolo, E. Stavrinidou, X. Strakosas, C. Tassone, D. M. Delongchamp, G. G. Malliaras, Structural control of mixed ionic and electronic transport in conducting polymers. *Nat. Commun.* **7**, 11287 (2016).
45. D. Khodagholy, J. Rivnay, M. Sessolo, M. Gurfinkel, P. Leleux, L. H. Jimison, E. Stavrinidou, T. Herve, S. Sanaur, R. M. Owens, G. G. Malliaras, High transconductance organic electrochemical transistors. *Nat. Commun.* **4**, 2133 (2013).
46. Y. Liu, J. Li, S. Song, J. Kang, Y. Tsao, S. Chen, V. Mottini, K. McConnell, W. Xu, Y.-Q. Zheng, J. B.-H. Tok, P. M. George, Z. Bao, Morphing electronics enable neuromodulation in growing tissue. *Nat. Biotechnol.* **38**, 1031–1036 (2020).
47. Y. Liu, J. Liu, S. Chen, T. Lei, Y. Kim, S. Niu, H. Wang, X. Wang, A. M. Foudeh, J. B.-H. Tok, Z. Bao, Soft and elastic hydrogel-based microelectronics for localized low-voltage neuromodulation. *Nat. Biomed. Eng.* **3**, 58–68 (2019).
48. M. Javadi, Q. Gu, S. Naficy, S. Farajikhah, J. M. Crook, G. G. Wallace, S. Beirne, S. E. Moulton, Conductive tough hydrogel for bioapplications. *Macromol. Biosci.* **18**, 10.1002/mabi.201700270 (2018).
49. C. M. Tringides, N. Vachicouras, I. de Lázaro, H. Wang, A. Trouillet, B. R. Seo, A. Elosegui-Artola, F. Fallegger, Y. Shin, C. Casiraghi, K. Kostarelos, S. P. Lacour, D. J. Mooney, Viscoelastic surface electrode arrays to interface with viscoelastic tissues. *Nat. Nanotechnol.* **16**, 1019–1029 (2021).
50. H. Wei, M. Lei, P. Zhang, J. Leng, Z. Zheng, Y. Yu, Orthogonal photochemistry-assisted printing of 3D tough and stretchable conductive hydrogels. *Nat. Commun.* **12**, 2082 (2021).
51. X. Su, X. Wu, S. Chen, A. M. Nedumaran, M. Stephen, K. Hou, B. Czarny, W. L. Leong, A highly conducting polymer for self-healable, printable, and stretchable organic electrochemical transistor arrays and near hysteresis-free soft tactile sensors. *Adv. Mater.* **34**, e2200682 (2022).
52. M. Das, D. Sen, N. U. Sakib, H. Ravichandran, Y. Sun, Z. Zhang, S. Ghosh, P. Venkatram, S. Subbulakshmi Radhakrishnan, A. Sredenschek, Z. Yu, K. J. Sarkar, M. U. K. Sadaf, K. Meganathan, A. Pannone, Y. Han, D. E. Sanchez, D. Somvanshi, Z. Sofer, M. Terrones, Y. Yang, S. Das, High-performance p-type field-effect transistors using substitutional doping and thickness control of two-dimensional materials. *Nat. Electron.* **8**, 24–35 (2025).
53. C. Cea, G. D. Spyropoulos, P. Jastrzebska-Perfect, J. J. Ferrero, J. N. Gelinas, D. Khodagholy, Enhancement-mode ion-based transistor as a comprehensive interface and real-time processing unit for in vivo electrophysiology. *Nat. Mater.* **19**, 679–686 (2020).
54. C.-G. Han, X. Qian, Q. Li, B. Deng, Y. Zhu, Z. Han, W. Zhang, W. Wang, S.-P. Feng, G. Chen, W. Liu, Giant thermopower of ionic gelatin near room temperature. *Science* **368**, 1091–1098 (2020).
55. J. Yin, S. Wang, T. Tat, J. Chen, Motion artefact management for soft bioelectronics. *Nat. Rev. Bioeng.* **2**, 541–558 (2024).
56. J. Peter, F. Ferraioli, D. Mathew, S. George, C. Chan, T. Alalade, S. A. Salcedo, S. Saed, E. Tatti, A. Quartarone, M. F. Ghilardi, Movement-related beta ERD and ERS abnormalities in neuropsychiatric disorders. *Front. Neurosci.* **16**, 1045715 (2022).
57. L. Yakovlev, N. Syrov, A. Miroshnikov, M. Lebedev, A. Kaplan, Event-related desynchronization induced by tactile imagery: An EEG study. *eNeuro* **10**, ENEURO.0455-22.2023 (2023).
58. Y. Meirovitch, H. Harris, E. Dayan, A. Arieli, T. Flash, Alpha and beta band event-related desynchronization reflects kinematic regularities. *J. Neurosci.* **35**, 1627–1637 (2015).
59. H. Shin, Z. Watkins, H. H. Huang, Y. Zhu, X. Hu, Evoked haptic sensations in the hand via non-invasive proximal nerve stimulation. *J. Neural Eng.* **15**, 046005 (2018).
60. L. Tian, B. Zimmerman, A. Akhtar, K. J. Yu, M. Moore, J. Wu, R. J. Larsen, J. W. Lee, J. Li, Y. Liu, B. Metzger, S. Qu, X. Guo, K. E. Mathewson, J. A. Fan, J. Cornman, M. Fatina, Z. Xie, Y. Ma, J. Zhang, Y. Zhang, F. Dolcos, M. Fabiani, G. Gratton, T. Bretl, L. J. Hargrove, P. V. Braun, Y. Huang, J. A. Rogers, Large-area MRI-compatible epidermal electronic interfaces for prosthetic control and cognitive monitoring. *Nat. Biomed. Eng.* **3**, 194–205 (2019).
61. R. Blau, A. Abdal, N. Root, A. X. Chen, T. Rafeedi, R. Ramji, Y. Qie, T. Kim, A. Navarro, J. Chin, L. L. Becerra, S. J. Edmunds, S. M. Russman, S. A. Dayeh, D. P. Fenning, R. Rouw, D. J. Lipomi, Conductive block copolymer elastomers and psychophysical thresholding for accurate haptic effects. *Sci. Robot.* **9**, eadk3925 (2024).
62. D. J. Lipomi, C. Dhong, C. W. Carpenter, N. B. Root, V. S. Ramachandran, Organic haptics: Intersection of materials chemistry and tactile perception. *Adv. Funct. Mater.* **30**, 1906850 (2020).
63. N. Zhuang, Y. Zeng, L. Tong, C. Zhang, H. Zhang, B. Yan, Emotion recognition from EEG signals using multidimensional information in EMD domain. *Biomed. Res. Int.* **2017**, 8317357 (2017).
64. A. Hyvärinen, Independent component analysis: Recent advances. *Philos. Trans. A Math Phys. Eng. Sci.* **371**, 20110534 (2013).
65. R. Yang, A. Dutta, B. Li, N. Tiwari, W. Zhang, Z. Niu, Y. Gao, D. Erdely, X. Xin, T. Li, H. Cheng, Iontronic pressure sensor with high sensitivity over ultra-broad linear range enabled by laser-induced gradient micro-pyramids. *Nat. Commun.* **14**, 2907 (2023).
66. X. Gu, L. Shaw, K. Gu, M. F. Toney, Z. Bao, The meniscus-guided deposition of semiconducting polymers. *Nat. Commun.* **9**, 534 (2018).
67. M. P. Seah, Summary of ISO/TC 201 Standard: VII ISO 15472: 2001—surface chemical analysis—x-ray photoelectron spectrometers—calibration of energy scales. *Surf. Interface Anal.* **31**, 721–723 (2001).
68. M. Ganji, A. Tanaka, V. Gilja, E. Halgren, S. A. Dayeh, Scaling effects on the electrochemical stimulation performance of Au, Pt, and PEDOT:PSS electrocorticography arrays. *Adv. Funct. Mater.* **27**, 1703019 (2017).

Acknowledgments: A.D. thanks D. Bhowmik from The Pennsylvania State University, University Park for the discussion on phase-separated Membraneless Organelles. A.D. and M.D. thank H. Ravikrishnan from The Pennsylvania State University, University Park for the help in electrical characterization of OECT. We also thank S. Kiemle, N. Wonderling, T. Zimudzi, M. Wetherington, and G. L. Tambourine from the Materials Research Institute, The Pennsylvania State University for atomic force microscopy, wide-angle x-ray scattering, Fourier transform infrared, Raman, and particle size characterization, respectively. A.D. thanks O. Mina, M. Quigley, and A. Ross from the Center for Quantitative Imaging, The Pennsylvania State University for μCT images. **Funding:** H.C. acknowledges the support provided by NIH (award no. R21EB030140), NSF (grant nos. 2319139 and 2309323), and Penn State University. A.D. acknowledges the support provided by NIH Training Grant T32NS115667, Diefenderfer Graduate Fellowship in Entrepreneurship, NSF I-Corps grant (2419142), and the Leighton Riess Graduate Fellowship at Penn State University. **Author contributions:** Conceptualization: A.D., A.M.C., and H.C. Data curation: A.D., M.A.S.B., W.L., B.P., and L.M. Formal analysis: A.D., M.A.S.B., S.P., M.D., A.M.A., Ji.Y., and L.M. Funding acquisition: X.H., H.C., and Sa.D. Investigation: A.D., E.G., Y.C., J.-Y.Y., M.A.S.B., W.L., J.M., M.D., A.M.A., Ji.Y., H.C., B.P., Sa.D., Sh.D., W.Z., A.M.C., and L.M. Methodology: A.D., E.G., Ju.Y., M.A.S.B., W.L., M.D., C.-H.C., W.Z., A.M.C., S.W., and L.M. Project administration: A.D., X.H., and H.C. Resources: A.D., Ju.Y., M.A.S.B., M.D., C.-H.C., H.C., B.P., Sa.D., and L.M. Software: A.D. and L.M. Supervision: A.D., X.H., C.-H.C., H.C., B.P., and SD. Validation: A.D., Ju.Y., M.A.S.B., X.H., W.L., M.D., C.-H.C., H.C., B.P., and A.M.C. Visualization: A.D., M.A.S.B., M.D., H.C., and L.M. Writing—original draft: A.D., E.G., H.C., and L.M. Writing—review and editing: A.D., E.G., Ju.Y., M.A.S.B., S.P., X.H., W.L., M.D., C.-H.C., H.C., B.P., Sa.D., S.W., and L.M. **Competing interests:** The authors declare that they have no competing interests. **Data, code, and materials availability:** All data and code needed to evaluate and reproduce the results in the paper are present in the paper and/or the Supplementary Materials. This study did not generate new materials.

Submitted 19 November 2025
Accepted 8 April 2026
Published 15 May 2026
10.1126/sciadv.aee0777

ScienceAdvances

Controlling thermoreversibility and hole conductivity in thermoresponsive ionic biogels using phase morphology for neurohaptics

Ankan Dutta, Md Abu Sayeed Biswas, Ethan Gerhard, Mayukh Das, Long Meng, Wanqing Zhang, Wenjie Li, Arantza Moreno Calva, Shakul Pathak, Jia-Yu Yang, Junyi Yin, Jordan Meyet, Shuvendu Das, Bed Poudel, Abu Musa Abdullah, Yuju Che, Cheng-Hsin Chuang, Jian Yang, Sihong Wang, Xiaogang Hu, Saptarshi Das, and Huanyu Cheng

Sci. Adv. **12** (20), eaee0777. DOI: 10.1126/sciadv.aee0777